The Gravimetric Geoid for Mexico: xGGM23

by

David Avalos-Naranjo

BSc Applied Mathematics, Universidad Autonoma de Aguascalientes.

A Thesis Submitted in Partial Fulfillment
of the Requirements for the Degree of

Master of Science in Engineering

in the Graduate Academic Unit of Geodesy and Geomatics Engineering.

Supervisor: Marcelo Santos, PhD., Geodesy and Geomatics Engineering

Examining Board: Michael B. Sheng, PhD., Geodesy and Geomatics Engineering
Cliff S. Shaw, PhD., Earth Sciences

This thesis is accepted by the Dean of Graduate Studies

THE UNIVERSITY OF NEW BRUNSWICK

March 2024

Abstract

The work presented in this thesis deals with the construction of a new gravimetric geoid model for Mexico. A large amount of terrestrial gravimetry collected up to year 2020 was processed in spectral combination with the satellite-derived geopotential model GOCO06s using the UNB's Stokes-Helmert technique. The geoid model complies with international standards of the regional geoid for North and Central America and its resolution of 2.5 arc minutes is coherent with the actual spacing in gravimetry data holdings for the country. It was found that the new geoid model agrees with the national vertical datum by 10 cm in standard deviation, which implies a significant improvement from previous models. Improvements are mainly due to the recent densification of terrestrial gravity surveys, refinements in the software code of the SHGeo package, and an optimization process to select the frequency on which the terrestrial input data takes over from the satellite source.

Dedication

To my mother.

Acknowledgements

To my professors and mentors, from UNB Dr. Petr Vanicek and Dr. Marcelo Santos, and from INEGI in Mexico, MSc. Antonio Hernandez-Navarro, my biggest gratitude for their continuing trust and support, offering sincere advice and a genuine example of passion for the science of Geodesy.

I would like to thank Dr. Robert Kingdon, Dr. Spiros Pagiatakis, Dr. Ismael Foroughi, Dr. Jianliang Huang and Dr. Michael Sheng for providing comments and fruitful discussions during my studies at UNB. Additional thanks to Silvia Witaker and Lisa Valenta for their kind attentions and practical guidance on administrative matters from the office of the GGE Department.

Thanks to the personnel at the National Institute of Statistics and Geography in Mexico (INEGI) involved in geoid modeling and gravity data collection who helped normalizing and validating several input datasets for geoid modeling: Raul Munoz-Abundes, Apolo Alavarado-Cortes, Marco A. Mendoza-Martinez, Manuel Sosa-Gaytan and Leticia Garcia-Santos. Similar, thanks to personnel at the US National Geodetic Survey, Dr. Kevin Ahlgren and Dr. Yan M. Wang, and the Canadian Geodetic Survey, Dr. Marc Veronneau for their help in collecting the most necessary information, as well as for sharing their expertise.

Table of Contents

List of Tables

List of Figures

List of Symbols

Symbol	Meaning	Chapters
a	major semi-axis of the reference ellipsoid	2
b	minor semi-axis of the reference ellipsoid	2
C	geopotential number	1
$\boldsymbol{C}$	covariance matrix of gravity observations	I
d	distance between two observed gravity values	I
g	magnitude of gravity	1,3
$\bar{g}$	mean gravity along the plumb line	1
G	Newton's gravitational constant	1,2,4
h	geodetic height	1,3,5
H^o	orthometric height	1,2,5
H^N	normal height	1,2
M	Mass of the Earth	1,2
N	geoidal height	1,2,4,5
Δg	gravity anomaly	2,3,I
$\Delta\boldsymbol{g}$	vector of gravity values observed	I
Δg^H	gravity anomaly in Helmert space	2,4
Δg_L^H	Reference gravity anomaly in Helmert space	2,4
Δg^{NT}	gravity anomaly in the No-Topography space	2,4,I
Δg^{SB}	simple Bouguer gravity anomaly	2
δg_{ATM}	atmospheric effect on gravity at a point	1
$\delta\Delta g_g^H$	High frequency gravity anomaly in Helmert space	2
δN_L^H	High frequency component of the geoid in Helmert space	2,4
δN^{z-n}	geoid height transformation from zero tide to tide-free system	2
δW	residual gravity potential	2
DTE^{NT}	direct effect of topography on gravity	2,4
DAE^{NT}	direct effect of the atmosphere on gravity	2,4
DTE^H	direct topographical effect on gravity from real space to Helmert space	2
DTE^C	effect on gravity of the condensed topography layer	4
DTE_L^H	low frequency DTE from real space to Helmert space	2

DAE^H	direct atmospheric effect on gravity from real space to Helmert space	2
k	Love number	2
	counter of gravity observations	I
K	Poisson kernel in spherical coordinates	2
	total of observed gravity values available	2
L	frequency limit for a spherical harmonic series	2,4
	Euclidean distance between two points	4
N_L^H	Low frequency component of the geoid in Helmert space	2
p_k	weight of the k-th observed gravity value	I
P_n	Legendre function	2
$\boldsymbol{P}$	vector of weight values of gravity observations	I
$PITE^H$	primary indirect topographical effect from real space to Helmert space	2
$PIAE^H$	primary indirect atmospheric effect from real space to Helmert space	2
Q_P	point on the telluroid	1
r	radial distance to a point	2,4
r_t	geocentric radius of a point on the Earth's surface	1,2,4
r_g	geocentric radius of a point on the geoid	1,2,4
R	mean radius of the reference ellipsoid	1,2,4
S	Stokes's kernel	2
$SITE_L^H$	low frequency SITE from real space to Helmert space	2
$SITE^{NT}$	secondary indirect topographical effect on gravity	2,4
$SIAE^{NT}$	secondary indirect atmospheric effect on gravity	2,4
$SITE^C$	effect on gravity of the condensed atmosphere layer	4
$SITE^H$	secondary indirect topographical effect from real space to Helmert space	2
$SIAE^H$	secondary indirect atmospheric effect from real space to Helmert space	2
T	gravity disturbing potential	1
T_L^H	Low frequency disturbing potential in Helmert space	2,4
U_0	normal gravity potential at the reference ellipsoid	1,2
U_P	normal gravity potential at a point	1
V^a	gravity potential from atmospheric mass	2
V^{ca}	gravity potential from the condensed atmospheric layer	2
V^t	gravity potential from topographic mass	2,4

V^{ct}	gravity potential from the condensed topography layer	2,4
W_0	gravity potential of the geoid	1,2,6
x	euclidean coordinate on the x axis	1
y	euclidean coordinate on the y axis	1
z	euclidean coordinate on the z axis	1
ε_{gqg}	geoid to quasigeoid separation	2,4
ε_n	ellipsoidal correction to the spherical approximation of gravity field	2,4
$\varepsilon_{\delta g}$	ellipsoidal correction to the radial approximation of the gravity vector	2,4
$\bar{\gamma}$	mean value of normal gravity along the plumb line	1
γ_0	normal gravity at the reference ellipsoid	2
φ	geodetic latitude	1,4
Φ_P	astronomical latitude	1
λ	geodetic longitude	1,4
Λ_P	astronomical longitude	1
Ω	solid angle related to latitude and longitude of a point	1,2,4
ψ	spherical angular distance between two points	2,4
σ	standard deviation	1,2,4,5,I
ρ_0	mean density of terrain ($2.67\ g/cm^3$)	2

Chapter 1: Introduction

A new gravimetric geoid model for Mexico is presented as the best existing solution in terms of coherence with the national vertical datum. It has been developed with implementation of the Stokes-Helmert technique on a large database of terrestrial gravity observations combined with information of the satellite geopotential model GOCO06s, which is in tune with conventional parameters for the future regional geoid for North and Central America.

The geoid model is a basic tool to take advantage of positioning based in Global Navigation Satellite Systems (GNSS) when the vertical dimension matters in mapping applications. This is the case of topographic modeling with sensors transported by airplane, like the laser-based systems (LIDAR), by satellite, like the radar-based TanDEM-X mission, or ground observations, like the modern surveying for detailed cadastral control (e.g. Navratil and Unger, 2011; Perez et al., 2020; Rizzoli et al., 2017). GNSS positioning for those and for many other systems delivers the observed value of geodetic height (h), while the required height for mapping applications is most commonly orthometric (H^O). Here the geoidal height (N) makes an easy transformation when it is known:

$$H^O \doteq h - N \, . \tag{1.1}$$

The approximation in this equation refers to the fact that H^O is reckoned along the direction of the gravity vector ($\boldsymbol{g}$), a different path than h and N (see Figure 1.1). Nonetheless, for most (if not all) applications, the inequality can be totally neglected because it hardly reaches a millimeter (Vaníček and Kleusberg, 1986).

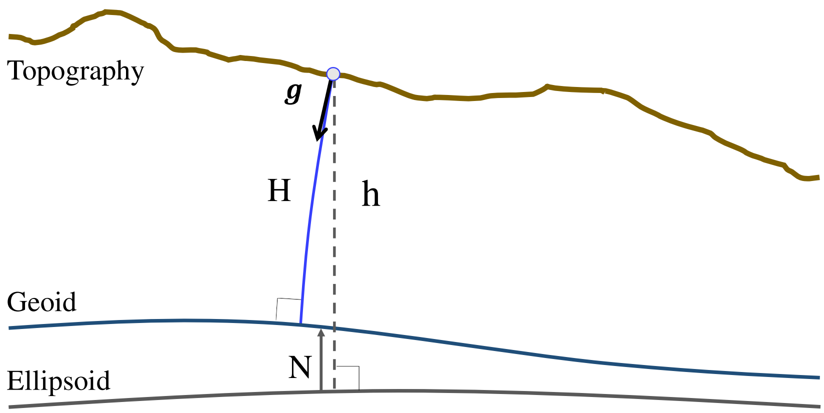

Figure 1.1. Relation among orthometric, geodetic and geoidal heights.

A geoid model is a numerical array of geoidal heights, corresponding to some specific grid of horizontal geodetic coordinates orderly stored in digital form. Computer systems are favored to handle geoid models in such way that any arbitrary location $P = (\varphi_P, \lambda_P)$, inside the spatial coverage of the model can be assigned with a corresponding geoidal height (N_P).

Now a days the geodetic height (h_P) can be obtained with precision of few centimeters under appropriate circumstances. This fact impulses some technological advancement, for instance, to produce mapping in high detail; however, the geoid models struggle to follow that level of precision. Generally speaking, current and near future mapping applications demand a centimetric accuracy in geoid models to access the maximum possible accuracy in orthometric heights.

It is a fact that the geoid can be calculated with sub-centimeter accuracy, implementing the Stokes-Helmert technique under the right circumstances of high-quality input gravity data and digital elevation models (Foroughi et al., 2018). For the test area of Auvergne, France, it was found that the geoid model produced with the current improvements of the Stokes-Helmert technique can be even more reliable and accurate than GNSS/leveling. This technique can be applied to any region of the world, but the accuracy of the result is tied to the quality of available gravity data and digital elevation models. Fortunately, now a days the last one mentioned is readily available for any region of the world in such conditions of quality that the impact of its errors is minimal on the geoidal height. It is in the availability of gravity data that one can find the biggest obstacle to reach a centimetric accuracy in the so-called gravimetric geoid. For the case of Mexico, the quantity and quality in gravimetric data has improved in recent times due to the evolution of methodology and implementation of reliable devises (INEGI, 2017). Nonetheless, the quality of the full gravity dataset accumulated during several decades in Mexico is heterogeneous: during decades of collecting gravity observations in the field, the method and sources used to determine the horizontal and vertical position of every observation location has changed several times. Chapter 3 contains a description of the most recent accumulation of gravity data in Mexico, suitable for geoid computations.

1.1 The geoid and the official vertical datum in Mexico

Currently in Mexico the geoid models available, like GGM10 or EGM2008, provide geoidal heights with typical error of two decimeters with respect to the GNSS/leveling data, referred to the official vertical datum. Such level of precision is sufficient for most common mapping applications, but the demand for higher precision is ever growing. Modern applications like flood-risk assessment, 3D cadaster or GNSS-based leveling would benefit for impact in a large amount of engineering projects.

Official vertical coordinates in Mexico are orthometric heights in Helmert's approximation (Heiskanen and Moritz, 1967) and its datum is NAVD88, as realized by a national adjustment of the first order leveling network in 2015 (INEGI, 2016). This realization of the vertical datum is often distinguished by the name NAVD88-Mx15. This datum is meant to represent an equipotential surface and ensures a reduction in distortions of one order of magnitude with respect to its predecessor NGVD29. The general accuracy of the NAVD88-Mx15 is believed to be around 10 cm nationwide. No specific evidence has been documented to support such precision. For a large and mountainous country like Mexico it is a major challenge to keep distortions near to zero.

In this situation, a gravimetric geoid model is expected to follow closely the official vertical datum of Mexico. Particularly, for the new geoid model presented in this dissertation it has been prepared an assessment with respect to the official Mexican datum, enriched with an assessment over the US territory, where there exists an experimental vertical datum realized from GNSS/leveling observations, as well as from a high resolution gravimetric geoid model, the xGeoid2020.

1.2 Research objective and contribution.

This research soughts to build a geoid model of national coverage for Mexico, expecting to find out the implications of recent advancement in the Stokes-Helmert geoid computation technique achieved at the University of New Brunswick (UNB). These improvements refer to better quality in the computation of topographical effects in gravity, a more stable process for downward continuation and a strategy to determine the optimal degree of resolution at which is best to combine the terrestrial and satellite gravity data sources.

The contribution of this research is the review and application of recent developments in the UNB's geoid computation software (Ellmann et al., 2005). It has been developed a program named gravgrid.c to calculate predicted mean gravity values, which conform a smoother field than that of the point values. The algorithm is based on inverse distance weighting, which formally handles a full covariance matrix to obtain a map of estimated error in the predictions (see Appendix A). It was developed a program named Helmert_ref.c to handle new geopotential models in format of spherical harmonic coefficients to obtain the reference maps of Helmert anomaly on the geoid and Helmert spheroid of any degree and order desired, referred to any optional W_0 value and adapted to any optional tide system: mean tide, tide free or zero tide. Other programs with smaller impact were developed as well to help users of the SHGeo software simplify operations, like normalizing the calculation for free air anomalies, the assembly of residual gravity anomaly on the geoid, and assembly the final geoid model. The new geoid model has an estimated precision of $\sigma = 10$ cm inside Mexico, twice as good as the model currently used by the national geodetic agency in Mexico, INEGI, and about 30% better than the latest experimental geoid model generated by the national geodetic agency of the US, the NGS. It is offered an interpretation of the results and some views about future work that may lead to an even better result.

1.3 Description of chapters

Details about the UNB Stokes-Helmert technique implemented to generate the new geoid model are displayed in Chapter 2. A whole new generation of data sources has been collected, checked and normalized to work with the UNB software package SHGeo (Ellmann et al., 2005). As it can be seen in Chapter 3, terrestrial gravity datasets from North and Central America had been assembled in a single and coherent file, along with digital elevation models, a modern geopotential model and survey results from precise NGSS and leveling. The work presented in this chapter is product of a group effort with INEGI's Department of the Geoid. Chapter 4 contains specific results, maps and statistic values obtained from every step taken from the application of the Stokes-Helmert technique. The final geoid model is described in detail, along with an assessment and discussion of results in Chapter 5, and lastly, a set of conclusions and recommendations in Chapter 6.

Next, in preparation to review the theoretical aspects of the UNB's application of the Stokes-Helmert technique, it is offered a brief overview of basic concepts and parameters.

1.4 Overview of basic concepts

Gravity (g) is the magnitude of acceleration produced by the gravitational field of the Earth, together with the effect of centrifugal acceleration (caused by rotational motion). The notation $g(x_P, y_P, z_P)$ specifies the gravity observed at a point P, referred by Cartesian coordinates to a geodetic reference frame, in such way that the gravity vector ($\vec{g}$) can be described as follows (Torge, 2001):

$$\vec{g}_P = -g_P \begin{bmatrix} \cos\Phi\cos\Lambda \\ \cos\Phi\sin\Lambda \\ \sin\Phi \end{bmatrix}. \tag{1.2}$$

Thus g is a scalar, positive quantity, observable with an absolute gravimeter in units of m/s^2. Angles Φ_P and Λ_P are observed with a zenith camera, in terms of astronomical latitude and astronomical longitude respectively, see Figure 1.2.

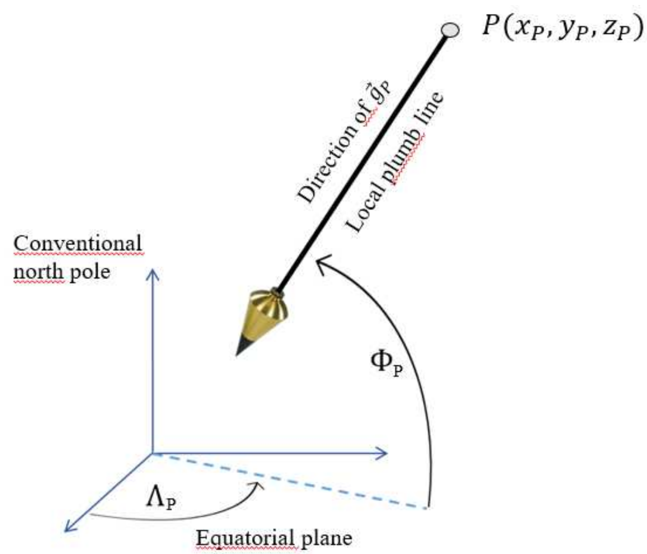

Figure 1.2: The gravity vector oriented from a geodetic reference frame.

Clearly $\vec{g}_P$ is perpendicular to the horizontal local level surface and (Φ_P, Λ_P) are closely perpendicular to the geoid for points with low height. The difference between

(Φ_P, Λ_P) and geodetic latitude and longitude (φ, λ) is known as deflection of the vertical. Alternatively, along this document, for reference of positions in spherical approximation, $g(r_P, \Omega_P)$ denotes the gravity at point P, where the vertical position (r_P) is determined as a radial distance from the origin of the reference frame (see Figure 1.2) and the horizontal position $\Omega_P = (\phi_P, \lambda_P)$ corresponds to geocentric latitude and longitude.

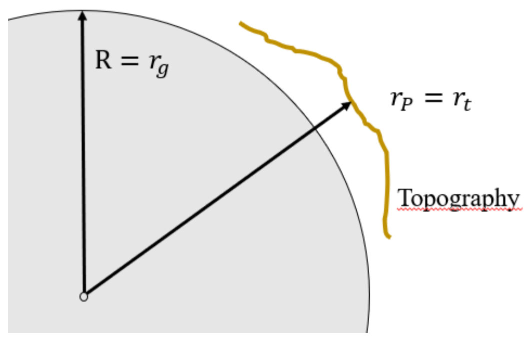

Figure 1.3: Schematics of a radial position in the spherical approximation, where the geoid (r_g) corresponds to the sphere of radius R (mean radius of the Earth) and the position of a point on the topography is $r_t(\Omega) = r_g(\Omega) + H^O(\Omega)$.

Any gravity vector observed on the topography represents the combined effect of all masses in the Earth, plus tide, which is the attraction exerted by celestial bodies like the Sun and Moon. In practice, it is a standard procedure to calculate and remove the tide effect from gravity observations. Hence, during this report the gravity vector is understood as the product of Earth's gravitation combined with the effect of Earth's centrifugal acceleration only.

The magnitude g_P of the gravity vector $\vec{g}_P$ can be split in three components: attraction from atmospheric masses (g_P^a), attraction from topographic masses (g_P^t) and attraction from the masses inside the geoid (g_P^g). It can be noticed intuitively that g_P^g is by far the largest component and g_P^t is larger than g_P^a. It is customary within the geodetic community to call g_P^t the *topographic effect* and g_P^a the *atmospheric effect*. Both can be calculated and removed from the observed value g_P in order to obtain an estimate of the gravity exerted by the geoid on the observation point.

Another concept, useful to dive into the Stokes-Helmert technique, is the *condensed topography*. It is an artificial mass distribution in which the topographic mass is conceived as a single, infinitesimally thin layer. The topographic mass is compressed down to this layer located touching the surface of the geoid. The gravity attraction from condensed topography is called *condensed topography effect*, it is actually similar to that of the real topography, but generally smaller as the orthometric height increases; i.e. due to the distance separating the gravity source and the observation point. See Figure 1.3 for reference.

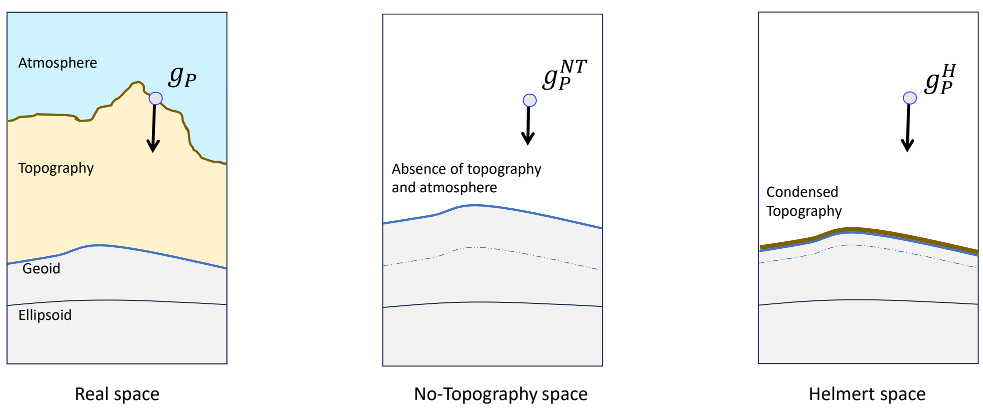

Figure 1.3: Scheme of mass distribution in three spaces and the magnitude of gravity.

The Earth's gravity potential over a point (W_P) is the number that corresponds to the sum of gravity values found along the plumb line, counted from the center of mass of the Earth to that point of interest. This potential is a scalar three-dimensional field which units are $m^2 s^{-2}$ and its mathematical expression is the following (Vaníček and Krakiwski, 1986):

$$g_P = -\frac{\partial W}{\partial H}|_P \text{ , or } W_P = -\int_{l=0}^{P} g\, dl \tag{1.3}$$

where l represents a distance measured from the center of mass to P, along the plumb line. The set of points in space where a constant potential value is found, form an equipotential surface. It is customary to indicate by W_0 the constant potential of the geoid and the difference between the gravity potential at P and the reference value W_0 is called the geopotential number (C_P).

$$C_P = W_0 - W_P = \int_0^P g\, dl \tag{1.5}$$

Height values derived from this expression, like the orthometric height (H^O) and the normal height (H^N), are known as physical heights, in units of meters.

$$H_P^O = \frac{C_P}{\bar{g}} \quad , \quad H_P^N = \frac{C_P}{\bar{\gamma}} \tag{1.6}$$

where $\bar{g}$ is the mean gravity observed along the plumbline from the geoid to P, and $\bar{\gamma}$ is the mean normal gravity (Moritz, 2000) calculated from the geodetic reference ellipsoid to a corresponding point Q_P on the telluroid (Heiskanen and Moritz, 1967).

The normal gravity field is generated by a reference potential U, for which, the reference ellipsoid is the equipotential surface $U_0 = W_0$. For point P, the difference between normal potential and real gravity potential is called the disturbing potential (Heiskanen and Moritz, 1967):

$$T_P = W_P - U_P \tag{1.7}$$

1.5 Fundamental parameters

The geoid model presented in this dissertation complies with the following adopted parameters, expecting to make it fully compatible with the future geoid for North and Central America, as recommended by the International Association of Geodesy, Sub-Commission 2.4c.

a) Product of the gravitational constant and the total mass of the Earth: $GM = 3.986044415 \times 10^{14} m^3 s^{-2}$. Same in the International Height Reference Frame (IHRF, Sanchez et al., 2021).

b) Geodetic reference frame: ITRF2008, epoch 2010.0.

c) Reference gravity potential: $W_0 = 62{,}636{,}856.0\ m^2 s^{-2}$. This is $4.85 m^2 s^{-2}$ smaller than the corresponding value U_0 at the GRS80 ellipsoid and larger than the conventional value adopted for the IHRF by $2.6 m^2 s^{-2}$.

Chapter 2: The Stokes-Helmert Technique

To an arbitrary position Ω corresponds a geoidal height $N(\Omega)$, which is directly proportional to disturbing potential (T) and inversely proportional to the normal gravity on the ellipsoid (γ_0) (Heiskanen and Moritz, 1967):

$$N(\Omega) = \frac{T(r_g, \Omega)}{\gamma_0(\varphi)} \tag{2.1}$$

where the disturbing potential is evaluated at the geoid level, represented by the radial distance r_g and the normal gravity on the ellipsoid is only latitude dependent. Units in this equation are m^2/s^2 over m/s^2. This mathematical relation is the well-known Bruns' formula, useful to compute the precise geoidal height under some circumstances. In this formulation the geoid is considered as the boundary of a body containing the mass of the Earth, including the atmosphere and terrain [e.g. Heiskanen and Moritz, 1967; Vaníček and Krakiwsky, 1986), just the way the geodetic reference ellipsoid is conceived as a geometric body containing the same mass (M).

The Stokes-Helmert technique deals with the correct application of the Bruns' formula, by rigorously transforming the environment of real gravity observations into an environment free of the influence of topography, i.e. the masses outside the geoid. Such space is advantageous also because it yields the possibility of continuing the gravity field downward from the topographic surface to the geoid, thanks to the harmonicity implied on the disturbing potential outside the geoid. In spherical approximation (Ellmann and Vaníček , 2007):

$$\nabla^2 T^H(R, \Omega) = 0 \ , \qquad (2.2)$$

where R is the mean radius of the Earth ($R = \frac{2a+b}{3}$), represented in Figure 1.3.

In Section 2.1 it is reviewed the set of operations required to transform gravity observations from the actual Earth's mass distribution to the Helmert space. Such transformation is often called Helmertization of the gravity field. Then, a strategy to perform a practical computation of disturbing potential and geoidal height from helmertized observations using a modified Stokes' integral, is reviewed in Section 2.2. Since all of this leads to obtain a precise cogeoid, i.e. a geoidal height in the Helmert space, then the final step in the Stokes-Helmert technique would be the transformation of the model back to the real space, as explained in Section 2.3.

2.1 Transition of actual gravity to the Helmert space.

Gravity ($g(r_t, \Omega)$) and gravity anomaly ($\Delta g(r_t, \Omega)$), as observed on the topographic surface, are influenced by the effect of atmospheric and topographic masses. These two effects are first calculated, then subtracted from the observation, and replaced by the effects of equivalent mass condensed in a thin layer placed at the geoid level. Such composition of effects -removing one and adding back a similar one- is called direct topographical effect (DTE^H) and direct atmospheric effect (DAE^H) (Vaníček et al., 1999):

$$DTE^H(r_t,\Omega) = \frac{\partial(V^t(r_t,\Omega) - V^{ct}(r_t,\Omega))}{\partial r} \ , \tag{2.3}$$

$$DAE^H(r_t,\Omega) = \frac{\partial(V^a(r_t,\Omega) - V^{ca}(r_t,\Omega))}{\partial r} \ , \tag{2.4}$$

where V^t is the gravity potential generated by topographic masses, V^a is potential from atmospheric mass, V^{ct} and V^{ca} are potential generated by the corresponding condensation layers.

Additionally, the secondary indirect effect produced by a shift in the position of geopotential surfaces when the topography and atmosphere are modified, must be considered. These terms, represented as SITE and SIAE respectively, are calculated as follows:

$$SITE^H(r_t,\Omega) = \frac{2}{R}(V^t(r_t,\Omega) - V^{ct}(r_t,\Omega)) \ , \tag{2.5}$$

$$SIAE^H(r_t,\Omega) = \frac{2}{R}(V^a(r_t,\Omega) - V^{ca}(r_t,\Omega)) \ . \tag{2.6}$$

In practice, all these effects are calculated in spherical approximation to reduce the complexity of mathematical expressions. In order to avoid biasing the solution due to these approximations, two corrections are generated (Vaníček et al., 1999): one accounts for the omission error due to leaving out the actual ellipticity of the Earth's shape in topographic effects (ε_n) and another accounts for misalignment of the gravity vector from a radial direction assumed in the spherical approximation ($\varepsilon_{\delta g}$).

A complete operation to helmertize gravity anomaly values observed on the topography is implemented as follows (Ellmann and Vaníček , 2007; Vaníček et al., 1999):

$$\Delta g^H(r_t,\Omega) = \Delta g(r_t,\Omega) + DTE^H(r_t,\Omega) + DAE^H(r_t,\Omega) + SITE^H(r_t,\Omega) + \\ + SIAE^H(r_t,\Omega) - \varepsilon_n(\Omega) + \varepsilon_{\delta g}(\Omega) \quad , \tag{2.7}$$

where DTE^H is the dominant term of the transformation. Importantly, DTE^H is function of the variable topographic density (e.g. Martinec et al., 1995; Huang et al., 2001). It is customary to handle units of $mGal = m/s^2 \times 10^{-5}$, in all the operations related to gravity anomaly. This units are suitable for the amplitude of variations observed on the Earth's surface. The use of a constant density value in computing topographic effects induces a potential error in the geoid model for a few centimeters in mountainous areas (Huang et al., 2001).

2.1.1 Gridding in the No-Topography space.

As it was mentioned above, the effect of topography and atmosphere can be calculated and removed from gravity observations. When this operation is performed, the resulting quantities correspond to the No-Topography space (Vaníček et al., 2004). Among the characteristics of the NT space, it is highlighted here the property of smoothness of its gravity field. In this work I use the so-called NT anomaly or Spherical complete Bouguer anomaly (Δg^{NT}) to calculate an estimate of the mean value of gravity anomaly over regular areas of specific resolution in latitude and longitude. In gravity field modeling, this process is commonly known as *gridding*, and the result is a digital model of estimated mean values covering the area of interest, free from data gaps.

Analogous to the expressions in the previous section, Δg^{NT} is obtained as follows:

$$\Delta g^{NT}(r_t,\Omega) = \Delta g(r_t,\Omega) + DTE^{NT}(r_t,\Omega) + DAE^{NT}(r_t,\Omega) + \\ SITE^{NT}(r_t,\Omega) + SIAE^{NT}(r_t,\Omega) - \varepsilon_n(\Omega) + \varepsilon_{\delta g}(\Omega) \ , \tag{2.8}$$

where,

$$DTE^{NT}(r_t,\Omega) = \frac{\partial V^t(r_t,\Omega)}{\partial r} \ , \tag{2.9}$$

$$DAE^{NT}(r_t,\Omega) = \frac{\partial V^a(r_t,\Omega)}{\partial r} \ , \tag{2.10}$$

$$SITE^{NT}(r_t,\Omega) = \frac{2}{R} V^t(r_t,\Omega) \ , \tag{2.11}$$

$$SIAE^{NT}(r_t,\Omega) = \frac{2}{R} V^a(r_t,\Omega) \ . \tag{2.12}$$

Taking advantage of the characteristic smoothness in Δg^{NT}, i.e., the reduced tilt changes in the surface, the amplitude of errors committed by the prediction method are certainly minimized. Moreover, the prediction of a mean gravity value is statistically more precise than any single point prediction. Section 4.1 and Appendix A contain details about the algorithm implemented to obtain predictions of the mean gravity anomaly, including the estimate of prediction errors.

From this point, in the description of the computation technique it is assumed that all quantities expressed in the equations are valid for point values as well as for mean values. In common practice, for the geoid computations performed at UNB, the mean value is obtained from averaging a set of point values calculated inside a cell-area of interest.

Now, in order to transit from Δg^{NT} to Δg^{H}, the gravity effects of condensed terrain are considered:

$$\Delta g^{H}(r_t,\Omega) = \Delta g^{NT}(r_t,\Omega) + DTE^{C}(r_t,\Omega) + DAE^{C}(r_t,\Omega) + SITE^{C}(r_t,\Omega) + SIAE^{C}(r_t,\Omega) \quad , \tag{2.13}$$

where the quantities with superscript C refer to the layer of condensed terrain.

The gridding procedure described above differs from those implemented before by e.g., Janak and Vaníček, 2005; Avalos-Naranjo et al., 2016b; Foroughi, 2018b. In those works, the observations were firstly transformed into Refined Bouguer anomaly; secondly, the gridding was applied to produce a model of Refined Bouguer anomaly; thirdly, the model was transformed back into a model of free-air anomaly, and lastly this model was transformed into Helmert anomaly applying simultaneously the mean effects of NT and condensed topography.

2.2 Downward continuation.

Once in the Helmert space, the behavior of gravity anomaly can be predicted in upward direction with the Poisson integral:

$$\Delta g^{H}(r_t\Omega) = \frac{R}{4\pi r_t}\int_{\Omega_0} \Delta g^{H}(r_g\Omega) K(r_t,\psi(\Omega,\Omega'),R)\, d\Omega' \quad , \tag{2.14}$$

where ψ is the angular distance between the point of interest Ω and the integration point Ω', function K is the Poisson kernel, and the quantity sought $\Delta g^{H}(r_g\Omega)$ is convolved with

K. Since the solution is implicit in the integral, $\Delta g^{H}(r_g\Omega)$ is obtained by approximation through an iterative process. The result is the estimated gravity field on the geoid. Details of this process are presented by Kingdon and Vaníček , 2010.

2.3 Modified Stokes integral.

The most recent Earth geopotential models (EGM) derived only from satellite gravimetry and satellite orbit analysis, are an excellent source to model the lower frequencies of the gravity field, and therefore, the lower frequencies of the geoid. One of these EGM is chosen as a pre-solved component of the geoid model in the Stokes-Helmert technique up to a certain resolution limit (L) expressed in terms of degree and order of the spherical harmonic expansion, on which they regularly are provided. The actual choice of this limit usually comes from specific studies of the accuracy in varying spectral resolution. According to Kvas et al., 2021, the high accuracy of GOCO06s spans in the spectrum up to degree and order 180 or 200. One of these values can be given to the parameter L, but in this study, it was implemented a strategy to determine L in function of the accuracy achieved in the geoid for the target area. The method followed is close to that proposed by Foroughi et al., 2016, creating geoid solutions with changing L, but keeping a fixed near-zone capsize. More details are expressed in Section 5.1.

The low frequency component of the geoid, called reference spheroid (N_L^H), is obtained in the same way as in equation 2.1, using as input a low frequency disturbing potential T_L^H, already transformed to the Helmert space. This Helmertization is achieved by adding a DTE_L^H and a $SITE_L^H$ to the spherical harmonic coefficients of the satellite EGM; i.e.,

$$T_L^H = T_L + DTE_L^H + SITE_L^H \quad , \tag{2.15}$$

where (Vaníček et al., 1995):

$$DTE_L^H = -\frac{G\rho_0 R}{2r}\int_{\Omega'} H'^2 d\Omega' + \tag{2.16}$$

$$+\frac{G\rho_0}{2}\sum_{n=2}^{L}\left(\frac{R}{r}\right)^{n+1}(n-1)\int_{\Omega'} H'^2 P_n(cos\psi)d\Omega' \quad .$$

In practice, this calculation is carried out from topographic models expressed in spherical harmonic coefficients to simplify the operations.

Additional details regarding the computation of T_L^H and its proper scale are provided in Vaníček and Kleusberg, 1987. Analogously, the Helmert field of reference gravity anomaly on the geoid ($\Delta g_L^H(r_g, \Omega)$) is obtained from T_L^H (Vaníček et al., 1995).

The complementary high frequency component of the geoid (δN_L^H) is obtained from a generalized scheme of the Stokes integral (Vaníček and Sjoberg, 1991). Firstly, the integral is fed with residual gravity anomaly values on the geoid ($\delta\Delta g_g^H$), which are obtained as follows:

$$\delta\Delta g^H(r_g, \Omega) = \Delta g^H(r_g, \Omega) - \Delta g_L^H(r_g, \Omega) \quad . \tag{2.17}$$

Secondly, the Stokes kernel is modified using truncation coefficients to allow the integral run on a spherical cap of radial distance ψ_0 and minimize the effect of the outer zone $(\Omega_0 - \Omega_{\psi 0})$ (Vaníček and Kleusberg, 1987). The integral split in the domain of near zone and far zone looks as follows:

$$\delta N_L^H(\Omega) = \frac{R}{4\pi\gamma_0(\phi)} \int_{\Omega' \in \Omega_{\psi 0}} S^*\big(\psi(\Omega, \Omega')\big) \delta\Delta g_g^H(\Omega') d\Omega' \tag{2.18}$$

$$+ \frac{R}{4\pi\gamma_0(\phi)} \int_{\Omega' \in (\Omega_0 - \Omega_{\psi 0})} S^*(\psi(\Omega, \Omega')) \delta\Delta g_g^H(\Omega') d\Omega'$$

where S^* is the modified Stokes kernel as function of the limit L.

2.4 Assembling the geoid.

The geoid in Helmert space is calculated assembling the lower and higher frequency components and finally, the primary indirect topographical and atmospheric effects ($PITE^H$ and $PIAE^H$) are added to obtain the geoid in real space.

$$N(\Omega) = N_L^H(\Omega) + \delta N_L^H(\Omega) + PITE^H(\Omega) + PIAE^H(\Omega) \ , \tag{2.19}$$

Where $N_L^H(\Omega) + \delta N_L^H(\Omega)$ is the cogeoid, and topographic effects depend also on the terrain density (Tenzer et al., 2004):

$$PITE^H(\Omega) = \frac{V^t(\Omega) - V^{ct}(\Omega)}{\gamma_0(\phi)} \ , \tag{2.20}$$

$$PIAE^H(\Omega) = \frac{V^a(\Omega) - V^{ca}(\Omega)}{\gamma_0(\phi)} \ , \tag{2.21}$$

2.5 Practical considerations.

It is convenient to note that implementing Stokes-Helmert technique on real data is challenging. Next, it is listed the set of considerations made in the case of the geoid computation for Mexico.

- Free-air gravity anomaly is commonly computed using orthometric height instead of normal height. This is the case of datasets handled by national agencies in the region of interest. In reaction to this situation, it was added a correction to normal gravity, known as geoid-to-quasigeoid correction (ε_{gqg}) (Heiskanen and Moritz, 1967):

$$\varepsilon_{gqg}(\Omega) = \frac{\partial\gamma}{\partial n}[H^N(\Omega) - H(\Omega)] \doteq \frac{-2}{R} H(\Omega)\Delta g^{SB} \ . \tag{2.22}$$

- Free air anomaly in the national databases of Mexico and North America includes an atmospheric correction, which is an equivalent operation as to applying DAE^H (Vaníček and Kleusberg, 1987). Besides, it is known that $SIAE^H$ contributes less than a centimeter to the geoid undulation worldwide; therefore, in the process of Helmertization both atmospheric effects are safely left out. Equation 2.8 was used as follows:

$$\Delta g^{NT} = \Delta g + DTE^{NT} + SITE^{NT} \quad . \tag{2.23}$$

- In this work all topographic effects are calculated using a constant density value $\rho_0 = 2.67\ \mathrm{g}/cm^3$. This is a standard value taken from the estimated mean density of the Earth's crust. Actual differences in rock density, specially where large areas of lower or higher density prevail, induce a change in the topographical effects calculated. Nonetheless, the total effect of this phenomena in geoidal height in low terrain reaches only one or two centimeters, while in mountainous areas the effect reaches several centimeters (Huang et al., 2001). This is the amplitude of potential error expected in the geoid model.

- As the geodetic reference frame used to parameterize all the computations uses the ellipsoid GRS80, the geoid models a surface of constant potential $W_0 = U_0 = 62636860.85\ m^2 s^{-2}$. This datum is adopted at the moment of producing the reference spheroid (N_L^H). Nonetheless, it is intended in this work to model a higher surface, characterized by the standard value adopted for the regional geoid of North America, $W_0^{NA} = 62636856.0\ m^2 s^{-2}$. For this reason, the Bruns' formula implemented to compute N_L^H was changed by a generalized version (Heiskanen and Moritz, 1967), in which the difference in potential is taken in consideration:

$$\mathrm{N} = \frac{T - \delta W}{\gamma_0} \quad , \tag{2.24}$$

where $\delta W = W_0^{NA} - U_0$.

- With regards to the construction of the reference spheroid N_L^H, the case of the geoid for Mexico requires an additional consideration. Given that the satellite-only gravity model selected is provided with a conventional zero-tide system (see Section 3.5), and the standard sought for the geoid models in North America is the tide-free, also called no-tide, system, then a corrective term was added. The transformation from zero tide to tide free system was implemented as follows (Ekman, 1989):

$$\delta N^{z-n} = -k(9.9 - 29.6 sin^2 \varphi) \text{ cm} , \tag{2.25}$$

where $k \approx 0.3$ is the Love number. This transformation ranges from -2.3 to 0 cm in the target region of the geoid model.

After reviewing the characteristics of input data for the geoid computation, next chapter includes a flowchart, useful to clarify the relation between software modules included in the SHGeo package, data sources and those theoretical elements reviewed here.

3 Chapter 3: Input data description

The strategy for precise geoid computation requires the availability of reliable topographic information like gravity observations on the terrain to create a realistic picture of the gravity field and digital terrain models to account for the actual mass distribution. This chapter summarizes the characteristics of these and other datasets collected, along with the tests and filters applied to facilitate the computation of gravity field models and independent geoidal heights for assessment.

3.1 Geodetic survey data

Geodetic surveys are essential for cross-validating input data as well as the final geoid model. Geodetic heights from GNSS positioning are useful to assess the precision of digital elevation models; orthometric heights from leveling are useful to estimate geoidal heights when combined with geodetic heights; and gravity values from gravimetry are essential to determine the field of gravity anomaly.

(a) **GNSS positions over Mexico.** A total of 94,618 of these records were provided by INEGI, some of which are created for referencing local topographic surveys (sites physically marked and identifiable) and the rest are to support the positioning of satellite or airborne imagery (not marked sites). For these datasets the uncertainty in horizontal coordinates is roughly $\sigma \approx 5$cm and in geodetic height it is nearly $\sigma \approx 9$cm (Armando

López-Delgado, personal communication, 2021). Reference frame is ITRF08, epoch 2010.0, meaning that the epoch was homogenized.

(b) **GNSS positions on benchmarks over Mexico.** 21000 records of benchmarks in Mexico with precise coordinates. The vertical datum of orthometric heights is NAVD88 from the national leveling adjustment of 2015 (INEGI, 2016). This datum is also named NAVD88-Mx15 to differentiate it from the leveling adjustment performed by NOAA in the early 1990's.

(c) **GNSS positions on benchmarks over the U.S**. 32276 benchmarks in the US with precise geodetic coordinates referred to IGS08 in observation epoch (not homogenized). The vertical datum of orthometric heights is NAVD88 detrended. It is well known that the NAVD88 contains a meter level distortion (e.g., Roman, 2010; Ahlgren et al., 2020), therefore the NGS applied a smooth correction surface to mitigate the distortion and delivered the corresponding orthometric heights. This dataset of orthometric heights is considered experimental and was created for the specific purpose of assessing the quality of geoid models (Ahlgren et al., 2020; Wang et al, 2022).

(d) **Geoid slope calibration lines in the U.S.** 220 benchmarks of the Geoid slope validation survey over Colorado (GSVS17) and 218 benchmarks in Texas (GSVS11) were provided by the NOAA's National Geodetic Survey (Smith et al., 2013, and van Westrum et al., 2021). These datasets contain absolute gravity observations, superior quality in orthometric height difference (minimally constrained to NAVD88) and GNSS positioning (van Westrum et al., 2021).

3.2 Digital terrain models

The digital terrain model xG20-DEM was provided by the NGS, as a research product expressly aiming to feed geoid computations for the region of North America. By using this model, the result of terrain effects is expected to be consistent with other geoid computation groups, like those in NRCAN and NOAA (Wang et al., 2022). This model covers latitude 0° to 85° and east longitude 170° to 350° with an original resolution of 3”x 3”. According to J. Krcmarik, 2021, it was made as an optimal combination of three sources: 3DEP (USGS, 2021), MERIT (Yamazaki et al, 2017) and TanDEM-X (Wessel et al. 2018). See Figure 3.1 for reference.

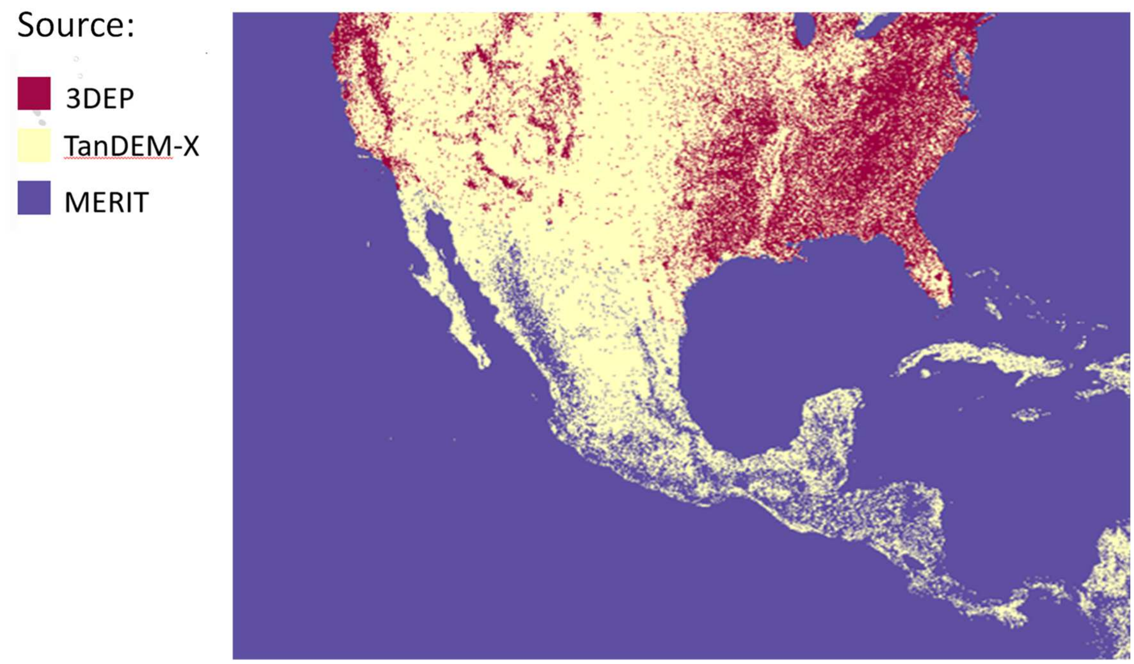

Figure 3.1: Map of the source selected to construct the xG20-DEM. Image provided by Krcmarik, 2021.

3.3 Terrestrial gravity datasets.

According to the recommendations of data coverage listed in the last chapter, the gravity dataset needed is enormous, involving 13 countries. Fortunately the task of seeking and integrating different sources has been worked out for many years by INEGI and the NGA (e.g. Avalos et al., 2016; Pavlis et al., 2010). Taking this advantage, it was possible to assemble the largest dataset ever used to feed a geoid computation for Mexico.

(a) **INEGI dataset.** INEGI provided 109,955 terrestrial observations inside Mexico. These have been accumulated since 1981 to 2020 in nearly homogeneous spacing of 2.5’, referred to the IGSN71. According to Alvarado Cortes, 2022 (personal communication), in most cases the expected error in gravity is about 0.3 mGal and about 3 m in orthometric height. Under this conditions, the typical error in free air anomaly is expected to be 1 mGal.

(b) **NGA dataset.** NGA provided 1.6 million records of terrestrial gravimetry covering the American countries within latitude 10° and 85°. From this dataset, 921346 records were found in the area of interest: latitude 4° to 46° and longitude 229° to 286°. Besides helping to cover the neighboring countries, this source provides a valuable coverage inside Mexico (72,915 points unevenly distributed), specially noting that it offers some densification by the northern border region on which other sources show scarce information.

(c) **Gravimetry in Yucatan.** CGS provided 9405 terrestrial and marine observations located at the northern coast of the Yucatan peninsula. This dataset was collected during years 1990s to map the gravimetric signature of the Chicxulub crater.

(d) **Gravimetry in Central America.** IGNCR and IGNTG provided 3686 terrestrial observations inside Costa Rica and Panama (Avalos et al., 2016).

3.4 Marine gravity datasets

For the ocean areas it was obtained the pre-modeled gravity anomaly from the last release by the research group at Denmark Technical University: model DTU21 (Andersen et al., 2023). This model provides a 1'x1' grid in global coverage, with gravity anomalies derived from analysis of satellite altimetry. It was decided to use data 15 km away from the coastline, due to the high uncertainty of the model in areas with large fluctuations of the sea level (e.g. Pujol et al., 2018; Andersen et al., 2017). In this version, the DTU model includes a terrestrial coverage taken from the EGM2008 (Pavlis et al., 2010). This terrestrial coverage was taken only for a small area of South America at the corner of the map in Figure 3.2.

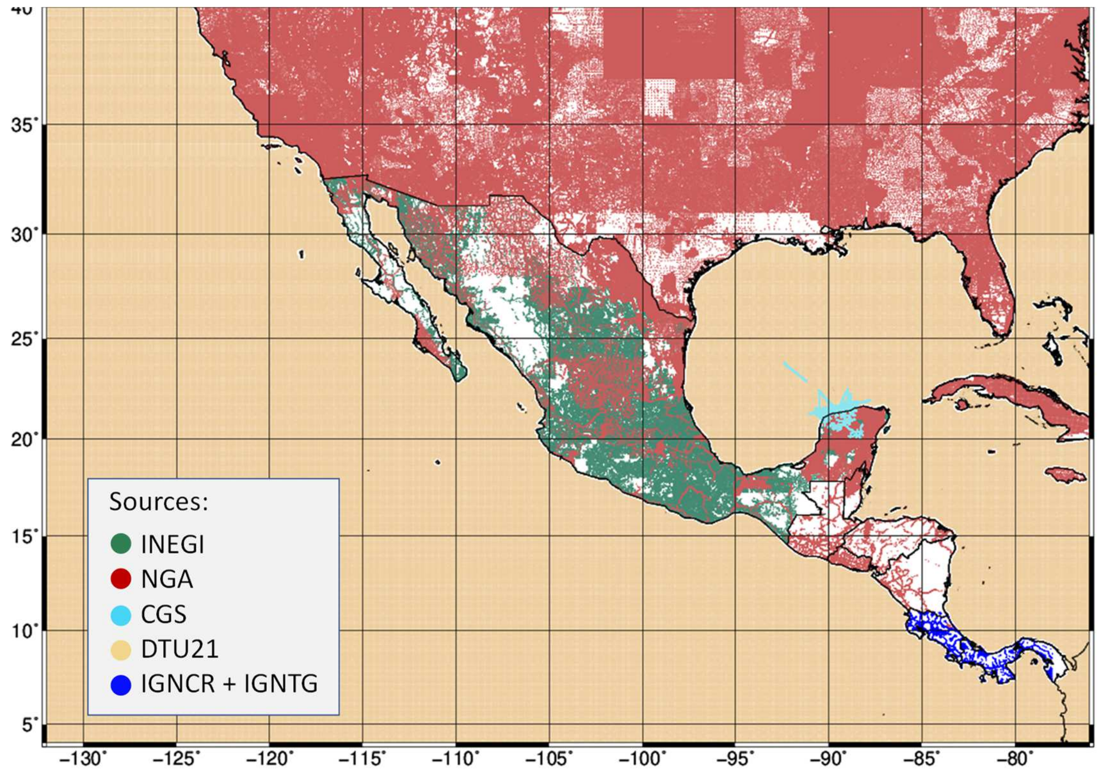

Figure 3.2. Terrestrial and marine gravity observations by source.

3.5 Satellite geopotential model

The absolute reference for the geoid model is obtained from the satellite-only gravity field model GOCO06s. According to Kvas et al., 2021, this model combines the most recent information accumulated by the satellite missions GRACE and GOCE, with additional contributions from orbit analysis of different missions like Swarm A+B+C, TerraSAR-X, TanDEM-X, CHAMP, GRACE and GOCE, and SLR observations to LAGEOS, LAGEOS 2, Starlette, Stella, AJISAI, LARES, LARETS, Etalon 1/2 and BLITS.

It is also relevant to highlight the fact that GOCO06s is the basic model used to construct the experimental Earth gravity models xG20RefA and xG20RefB, which in turn, were the base to produce the latest experimental geoid models for North America, by NOAA and the NRCAN (Wang et al., 2022). The selection of GOCO06s in this work ensures full compatibility in the lower frequencies among the national geoid models in the region.

3.6 Input data normalization

It is always convenient to perform a general check on the characteristics and quality of the datasets obtained to make sure these are appropriate for geoid modeling. Besides the issues of data formatting, the actions taken to verify the quality and parameterization are explained next.

3.6.1 Surface gravity anomaly

Free air gravity anomaly on the topographic surface ($\Delta \mathrm{g}^{FA}(r_t, \Omega)$), used as input in equation 2.7, was calculated using the reference GRS80 (Moritz, 2000) as follows:

$$\Delta g^{FA}(r_t, \Omega) = g(r_t, \Omega) - \gamma(H, \Omega) + \delta g_{ATM}(r_t, \Omega) \tag{3.1}$$

where

$$\gamma(H,\Omega) = \gamma(r_e,\phi) + \frac{\partial\gamma(r_e,\phi)}{\partial h}H(\Omega) + \frac{1}{2}\frac{\partial^2\gamma(r_e,\phi)}{\partial h^2}H^2(\Omega) \tag{3.2}$$

is the normal gravity, and δg_{ATM} is the atmospheric correction computed by:

$$\delta g_{ATM}(r_t,\Omega) = 0.8658 - 0.00009727 * H(\Omega) + 0.000000003482 * H(\Omega)^2 \tag{3.3}$$

All these calculations were performed using the orthometric height provided by the gravity datasets.

3.6.2 Terrain elevation model.

According to J. Krcmarik (2021), the precision of the model xG20-DEM is 1 to 3 meters over the conterminous U.S. territory. In order to determine the precision over Mexico it was combined the geodetic height from the 48,682 GNSS coordinates available and combined it with geoidal height from the GGM10, which has a precision $\sigma \approx 22$cm (Avalos et al., 2010), to obtain orthometric heights of uncertainty well below half meter. The resulting error estimate is presented in Table 3.1, clustering the statistics by the type of terrain.

Table 3.1: Statistics of the error estimate for the terrain model xG20-DEM.

DEM error [m] by type of terrain	Flat	Hills	Mountains	Total 48683p
mean	0.2	2.5	4.8	1.2
sigma	2.5	5.5	8.9	4.7
max	78.4	38.0	76.9	78.4
min	-13.4	-23.8	-34.8	-34.8

The assessment by terrain classification allows noticing the negative impact of roughness on the precision of the model. I notice the standard deviation of the total error observed is below 5 m and it is 10% to 20% better than the figures presented in a previous assessment under the same conditions for models SRTM4.1, TanDEM-X and CEM3 (Mendoza and Avalos, 2018). Figure 3.3 shows the map of heights in the area of interest.

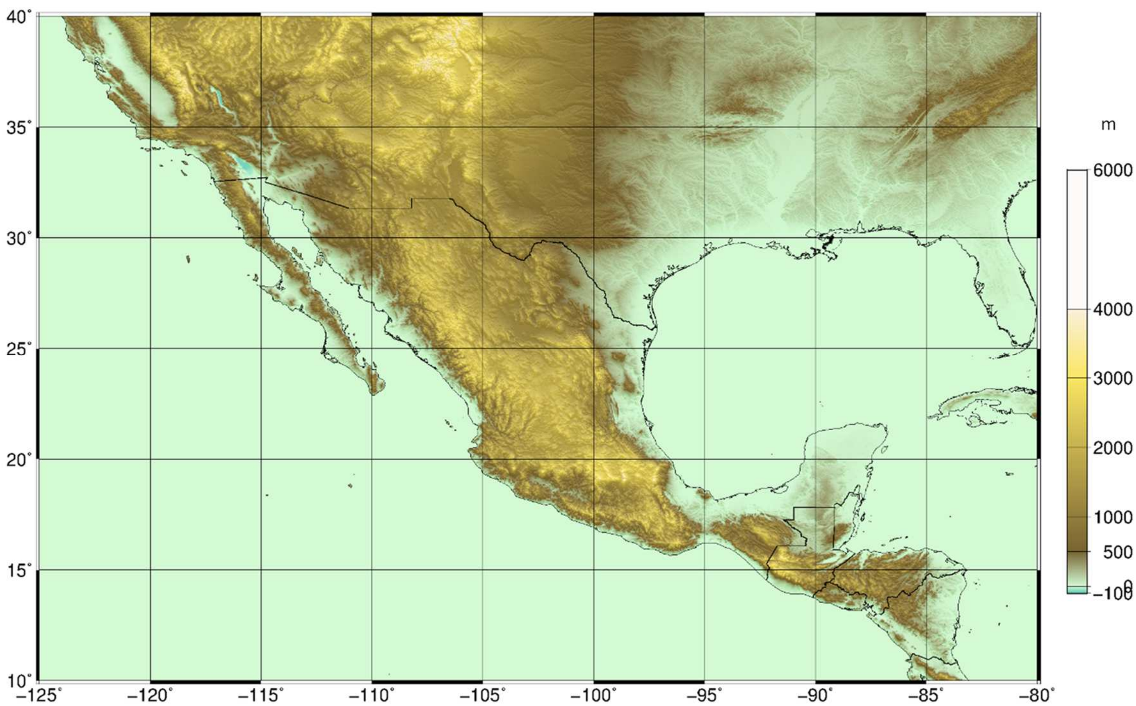

Figure 3.3. Map of orthometric height from the model xG20-DEM.

3.6.3 Validation of gravity records

From the total terrestrial gravity records collected, 6260 were labelled as outliers due to one or more of the following conditions.

- The height in the record disagrees by more than 100 m from the digital elevation model.

- Records with gravity value not referred to the topographical surface.
- Duplicate records.
- Records with no valid input in fields like gravity observed, latitude/longitude or height.
- Records exceeding clearly any local and regional trends and ranges of refined Bouguer anomaly under a visual inspection.
- Records with error larger than 4σ, in the context of comparing the modeled mean NT anomaly to the point values used as a source for modeling in a first loop.

After removing outliers, the definitive gravity dataset was composed of 1,038,789 records of terrestrial observations. The map of these records shows no visible difference from the map in Figure 3.4.

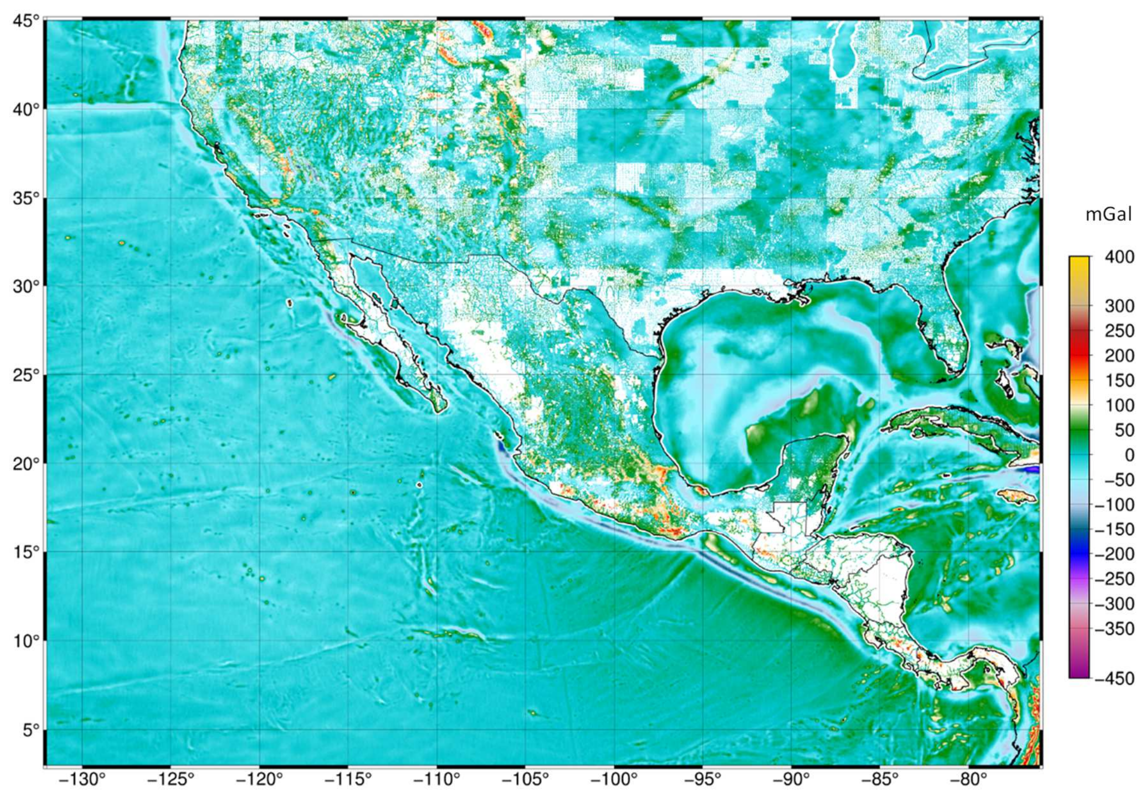

Figure 3.4: Point observations of free air gravity anomaly collected and normalized.

Table 3.2: Statistic values of the free air anomaly observations.

Statistic	Δg^{FA} terrestrial	Δg^{FA} marine
mean	-0.946	-10.181
sigma	32.441	27.589
max	364.513	187.500
min	-162.804	-246.900

3.7 Data flow diagram.

In order to help relating the concepts reviewed in Chapter 2 and the data sources, figures 3.5, 3.6 and 3.7 present a data flow diagram. Only some program names are included in the diagram. A full description of the SHGeo software is available in the Users' manual (Ellmann et al., 2005).

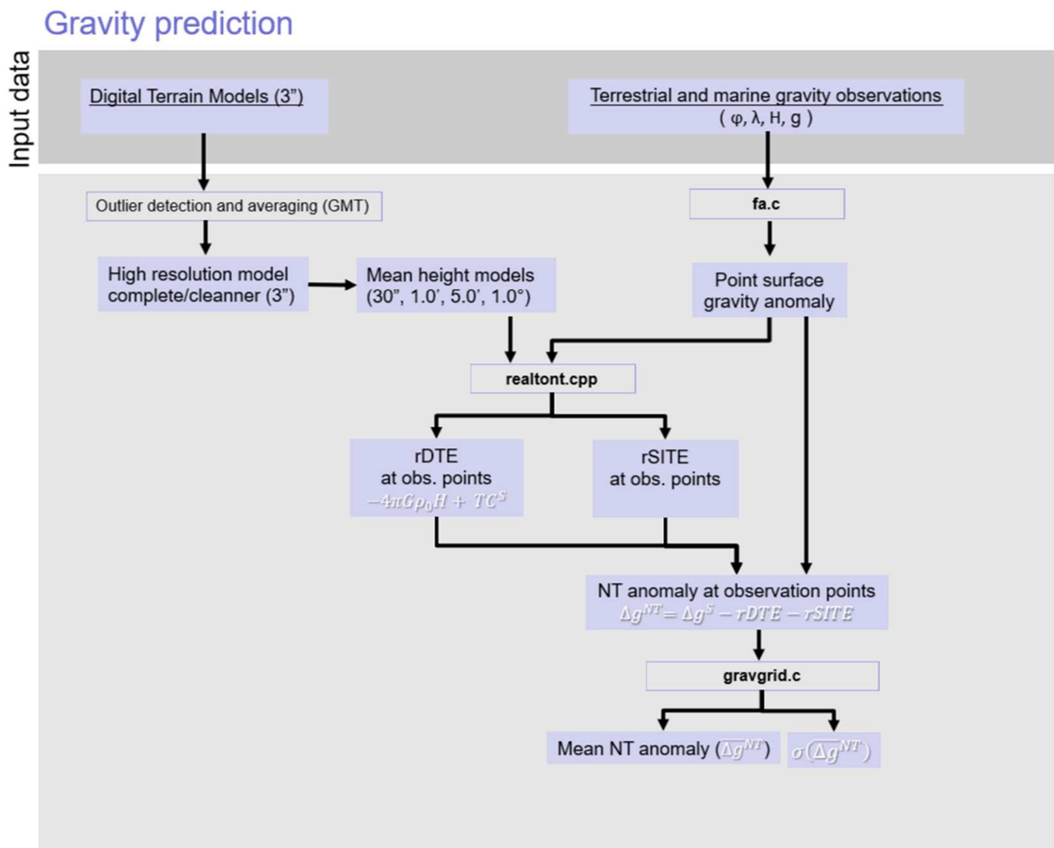

Figure 3.5: Data flow of the first computation stage, including the gridding process. Program names fa.c, realtont.cpp and gravgrid.c are part of the SHGeo software package.

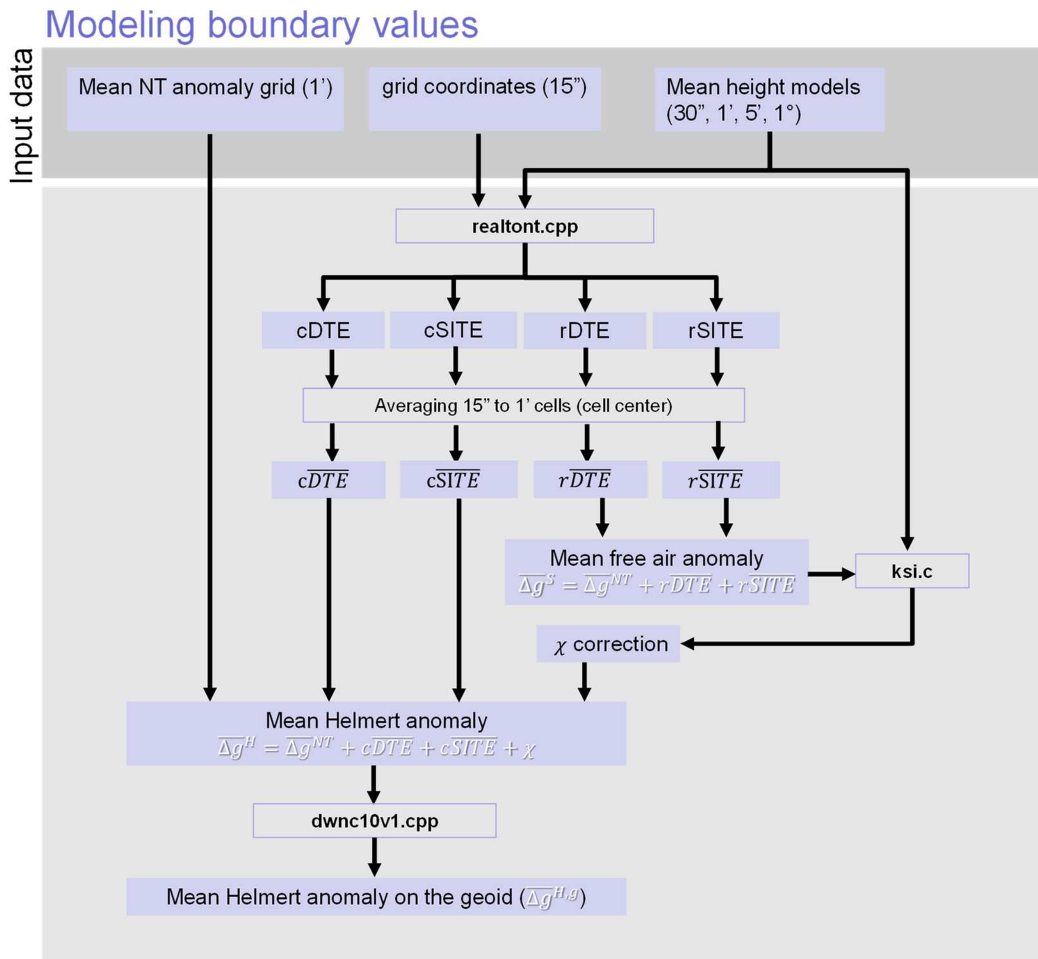

Figure 3.6: Data flow of the second computation stage, dealing with mean values related to cell areas. Program names realtont.cpp, ksi.c and dwnc10v1.cpp are part of the SHGeo software package.

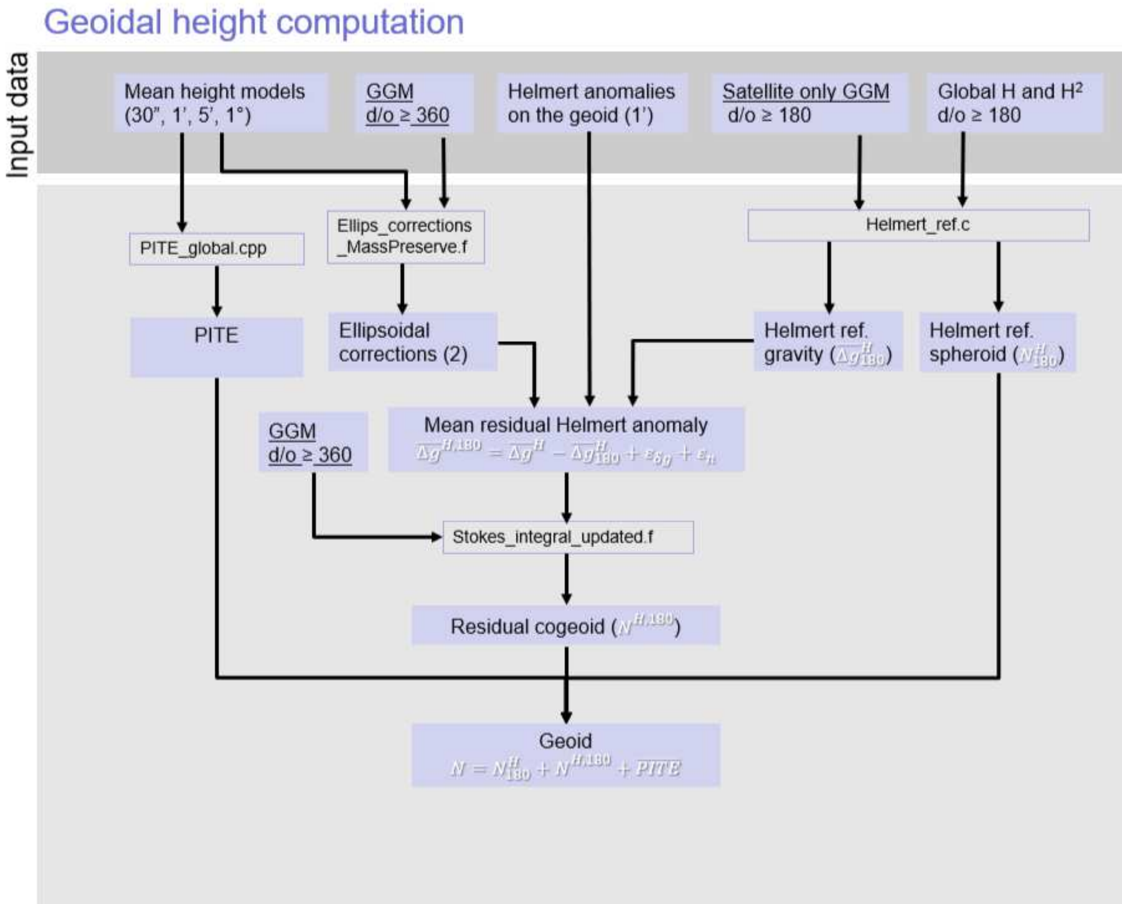

Figure 3.7: Data flow of the third computation stage. From Helmert gravity anomaly values on the geoid to the geoid model. Program names PITE_global.cpp, Ellips_corrections_MassPreserve.f, Helmert_ref.c and Stokes_integral_updated.f are part of the SHGeo software package.

Chapter 4: Results

This chapter presents the results of the geoid computation process, step by step. Starting with the treatment of free air anomaly to transform the dataset of scattered observations into a digital model of mean gravity anomaly. The mean values sought correspond to regular areas of 2.5 arc minutes in latitude and longitude. This resolution is in agreement with the most common spacing found in the INEGI gravity dataset. Only a few areas in Mexico contain denser observations.

4.1 Gravity prediction in the NT space.

The general strategy to obtain a digital model of predicted mean gravity values in every cell of 2.5’x2.5’ consists of several steps (see Figure 4.1). First of all, it is sought to make sure the gravity field on which the predictions are implemented is as smooth as possible. Following the idea of transforming free air gravity anomaly into refined Bouguer anomaly (Janak and Vaníček , 2004), it was decided to compute the complete spherical Bouguer anomaly as it is prescribed in Vaníček et al. (2004). The computation of this gravity anomaly is equivalent to having transformed the real space into the No-Topography space (NT space). Therefore, the complete spherical Bouguer anomaly is also called the NT-anomaly (Δg^{NT}).

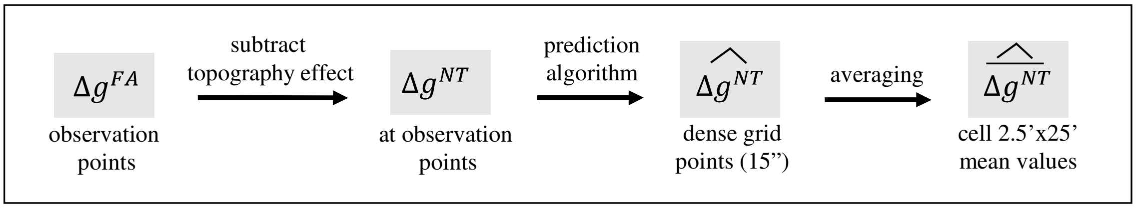

Figure 4.1: Algorithm followed to generate a digital model of mean gravity values.

Previous work has demonstrated the effectiveness of this strategy (Foroughi, 2019). Next sections contain details about the transformation implemented to obtain observed values of NT-anomaly and details about the prediction algorithm constructed.

4.1.1 Subtracting the effect of global topography.

Point observations of gravity anomaly were transformed to the No-Topography space (Δg^{NT}) by computing and removing the effect of topography. Following the formulation derived by Vaníček et al., 2004, equation 53, assuming a standard topographic density and neglecting corrective terms of small amplitude, it was applied as follows:

$$\Delta g^{NT}(r_t,\Omega) = \Delta g^{FA}(r_t,\Omega) - DTE^{NT} - SITE^{NT} \tag{4.1}$$

where DTE^{NT} is the gravity attraction of the global topography, equivalent to g^t in different reports, and $SITE^{NT}$ is the secondary indirect topographical effect experienced in the NT space, accounting for the effect on gravity due to vertical displacement of geopotential surfaces when the effect of topographic masses is removed. For practical computations this is the operation performed:

$$DTE^{NT}(r_t,\Omega) = \frac{\partial V^t(r_t,\Omega)}{\partial r} = -4\pi G\rho_0 H(\Omega) \tag{4.2}$$

$$+ GR^2\rho_0 \iint_{\Omega_0} \int_{r_t}^{r_t'} \frac{\partial L^{-1}(r_t,\Omega,r_t',\Omega')}{\partial r} dr_t' d\Omega'$$

and

$$SITE^{NT} = \frac{2}{r_g} V^t(r_t,\Omega) = \frac{2G\rho_0}{r_g} \iint_{\Omega_0} \int_{r_t}^{r_t'} L^{-1}(r_t,\Omega,r_t',\Omega') r_t'^2 dr_t' d\Omega' \tag{4.3}$$

where L is the distance between points (r_t,Ω) and (r_t',Ω'),

$$L(r_t,\Omega,r_t',\Omega') = \sqrt{r_t^2 + r_t'^2 - 2r_t r_t' \cos(\psi)} \tag{4.4}$$

and, $\cos(\psi) = cos\varphi cos\varphi' + sin\varphi sin\varphi' \cos(\lambda - \lambda')$ where ψ is the angular distance between the geocentric directions $\Omega = (\varphi, \lambda)$ and $\Omega' = (\varphi', \lambda')$.

Both effects were calculated in point mode to perform the transformation of scattered observations, but also in grid mode of resolution 15 arc seconds to produce digital models of mean effect over cell areas of 2.5 x 2.5 arc minutes. See Table 4.1 and figures 4.2 and 4.3 to learn about the magnitudes obtained as mean values.

Table 4.1: Statistical values for topographical effects on surface gravity, calculated as mean values in cell areas of 2.5 x 2.5 arc minutes.

Statistic	DTE^{NT}	$SITE^{NT}$
mean	55.586	-96.059
sigma	69.553	16.045
max	518.944	-72.286
min	15.592	-148.419

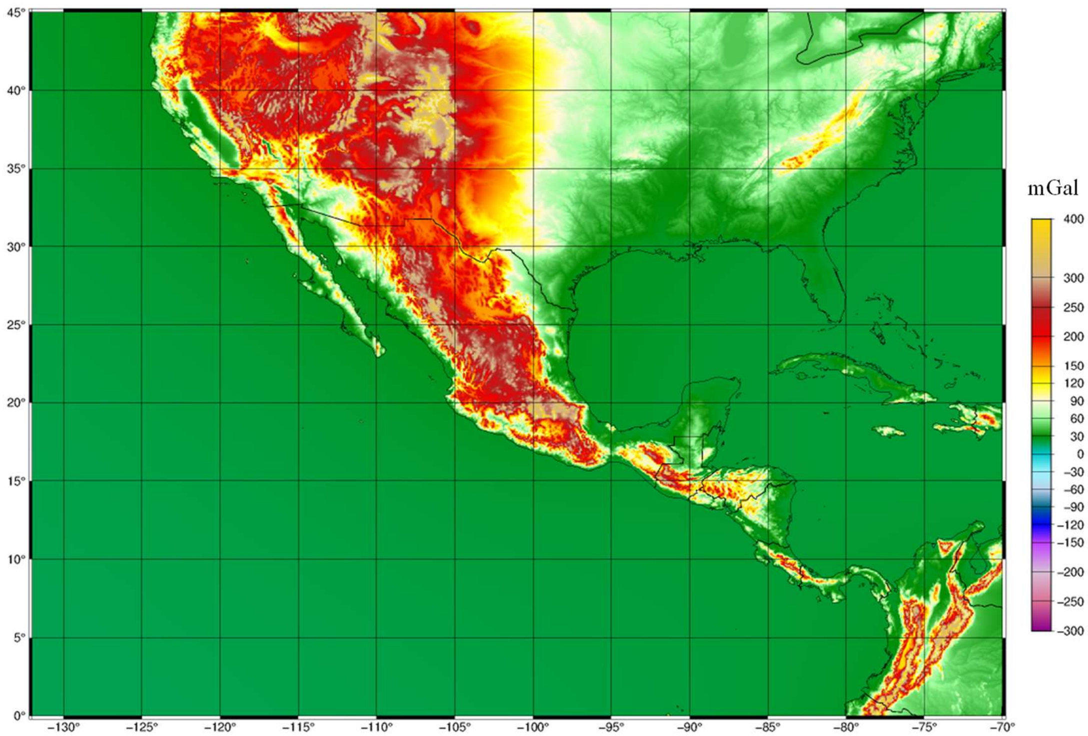

Figure 4.2: Map of the effect of topography on gravity at the surface (DTE^{NT}).

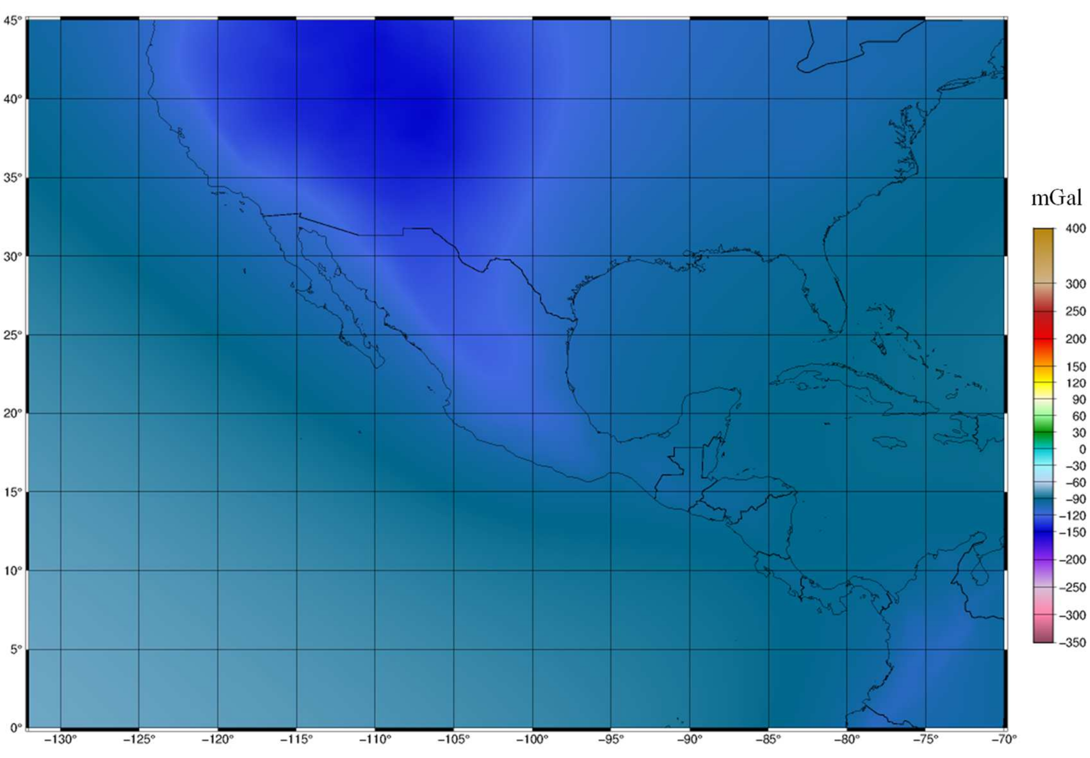

Figure 4.3: Secondary indirect topographical effect in the NT space ($SITE^{NT}$).

4.1.2 Gravity prediction algorithm.

Once the gravity field of the observations is as smooth as the NT space, the prediction process can be implemented with a significant reduction of the risk to commit large errors. According to the scheme presented in Figure 4.1, the second step is the prediction of gravity values on a dense grid of points regularly spaced. To establish such densification, the target points can be the cell-center of cell areas 10 or more times smaller than the 2.5', so that the sample is significant for averaging. The process of predicting gravity values is commonly performed by interpolation using some ready-made software, however, in this work it was decided to build a new piece of software to implement a robust algorithm capable to handle formal uncertainties. In this way, the output would not only be the matrix of estimated mean values, but also the matrix of uncertainty associated. This algorithm was provided by Dr. Petr Vaníček (2022, personal communication). See Appendix I for details about the process of gravity prediction. Figures 4.4 and 4.5 present the map of the resulting gravity field model and its related uncertainty.

Table 4.2: Statistical values for complete spherical Bouguer anomaly (Δg^{NT}).

Statistic	Δg^{NT}	$\sigma(\Delta g^{NT})$
mean	35.801	0.795
sigma	53.826	0.595
max	238.477	20.412
min	-223.477	0.458

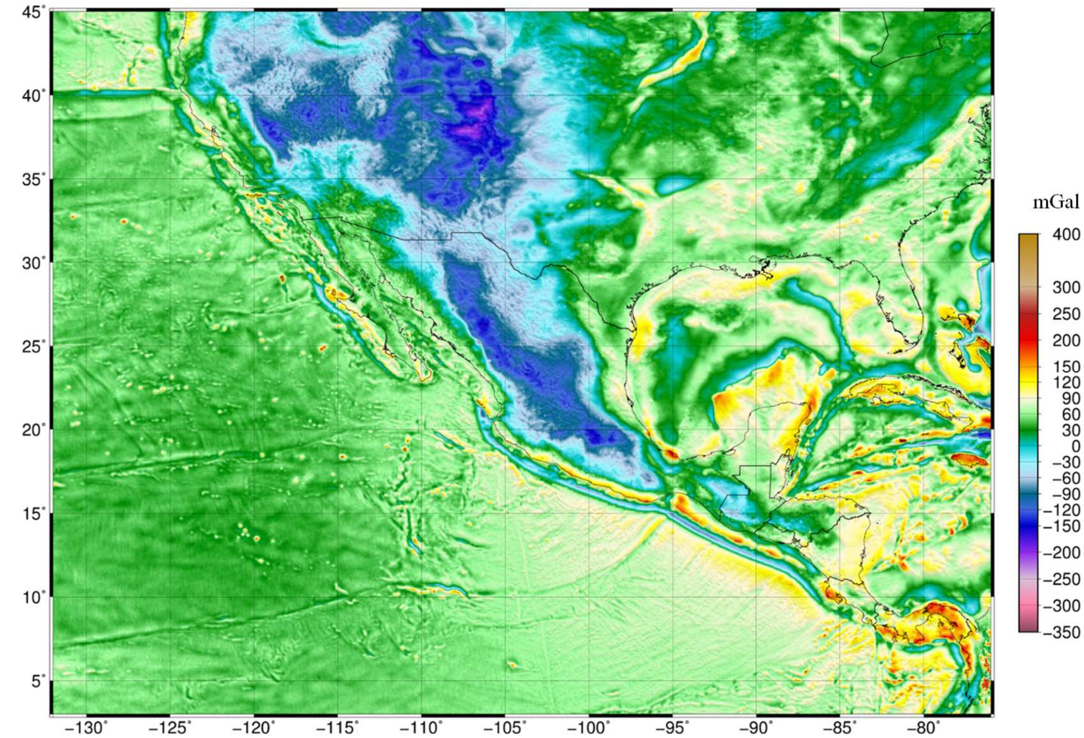

Figure 4.4: Map of mean spherical complete Bouguer anomaly.

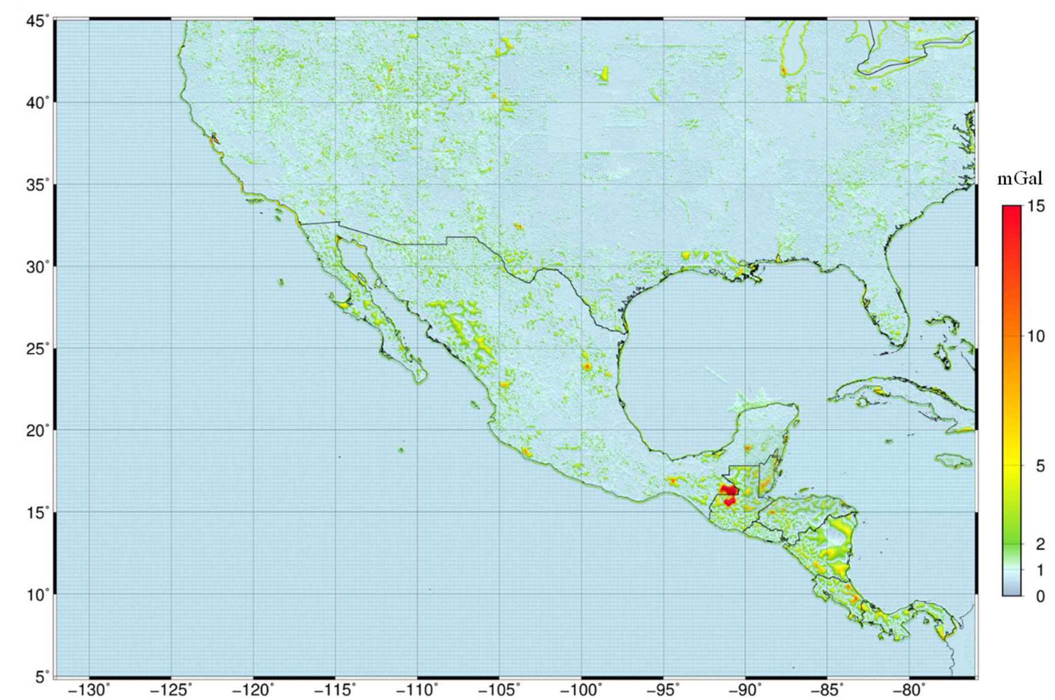

Figure 4.5: Standard deviation of the predicted mean spherical complete Bouguer anomaly.

It is clear in Figure 4.5 that the maximum uncertainty occurs around the border between Mexico and Guatemala. This is expected since the area contains the largest gap in the coverage of terrestrial gravity.

4.2 Gravity anomaly in the Helmert space.

Gravity anomaly in the NT space is transformed into the Helmert space by adding the effects of condensed topography (e.g., Tenzer et al., 2003; Yang et al., 2004). This effect is analog to the NT-effects defined before, with the topographic mass concentrated on a thin layer placed directly on the geoid. Such dense layer produces a gravity attraction similar to the effect of real topography. Adopting the second Helmert's condensation scheme, the NT anomaly computed in the previous section requires the addition of condensed topography effects: DTE^C, $SITE^C$ and the geoid-to-quasigeoid correction (ε_{gqg}) (e.g., Vaníček et al., 1999; Ellmann and Vaníček , 2007).

$$\Delta g^H(r_t, \Omega) = \Delta g^{NT}(r_t, \Omega) + DTE^C(r_t, \Omega) + SITE^C(r_t, \Omega) + \varepsilon_{gqg} \tag{4.5}$$

where ε_{gqg} was computed according to equation 2.22.

Table 4.3: Statistical values for topographical effects on the surface gravity. Units mGal.

Statistic	DTE^C	$SITE^C$	ε_{gqg}
mean	55.969	-97.196	-0.013
sigma	69.541	16.535	0.037
max	446.112	-72.291	0.174
min	18.072	-148.229	-0.407

The Helmert space is adequate to downward continue the gravity anomaly field from the surface to the geoid level. In this work it was applied the Jacobi iterative method as described by Kingdon and Vaníček , 2011. The iterations in this method start using the same input grid as approximate solution and stop using a relaxed tolerance based on the condition number of the matrix containing the Poisson kernel. The following figures, 4.6 and 4.7, present the resulting model of Helmert anomaly on the surface and the contribution of the downward continuation process.

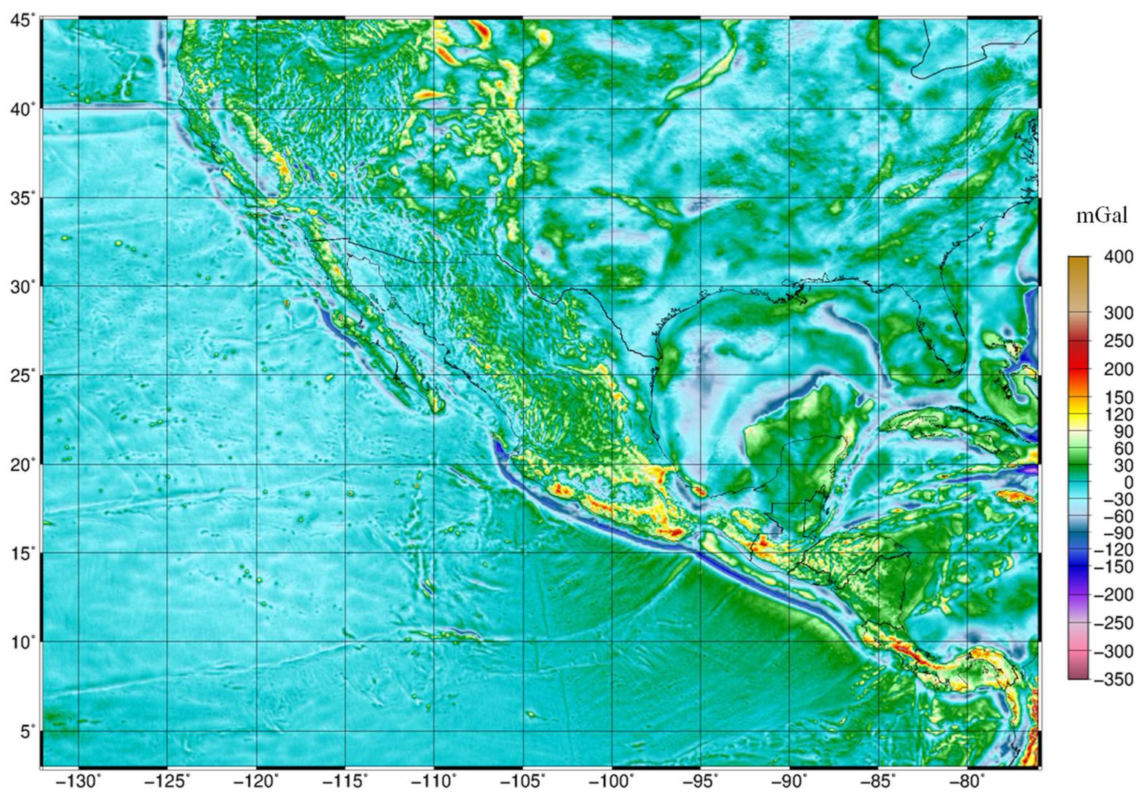

Figure 4.6: Map of Helmert gravity anomaly on the topography.

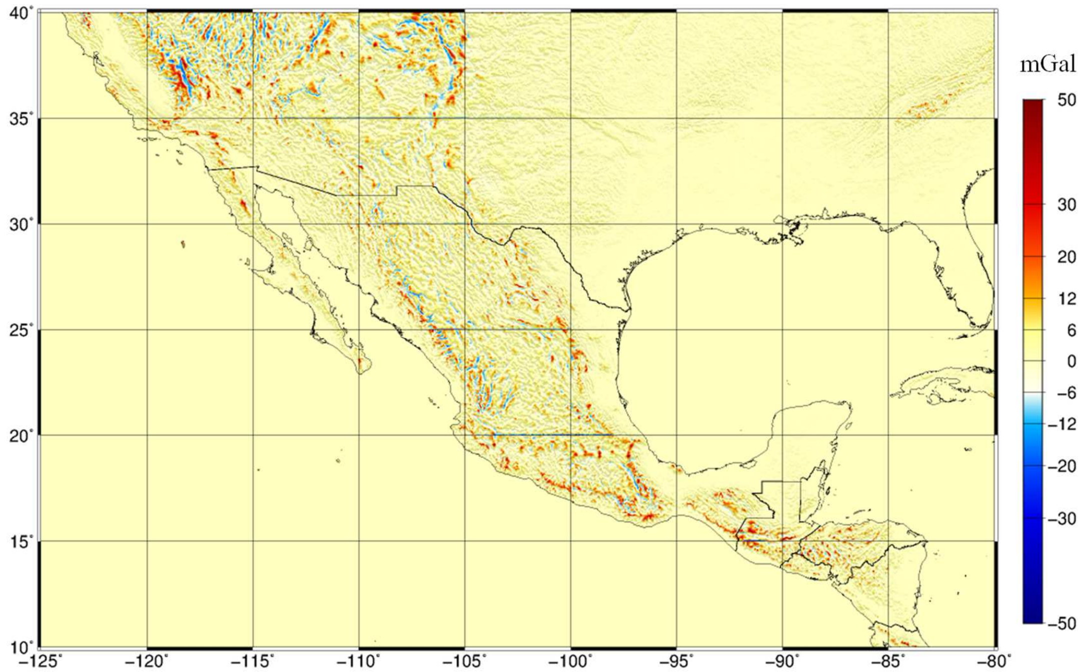

Figure 4.7: Map of the contribution from the downward continuation process.

Table 4.4. Statistical values for the Helmert gravity anomalies on the topography (r_t) and the geoid (r_g) before ellipsoidal corrections. Units mGal.

Statistic	$\Delta g^H(r_t, \Omega)$	Contribution of the downward continuation
mean	-2.693	0.222
sigma	30.848	2.558
max	294.362	54.296
min	-241.335	-36.158

Once the gravity anomaly has been transferred to the geoid level, two ellipsoidal corrections were added (see equation 2.7): the ellipsoidal correction for the gravity disturbance ($\varepsilon_{\delta g}$) and ellipsoidal correction for the spherical approximation (ε_n).

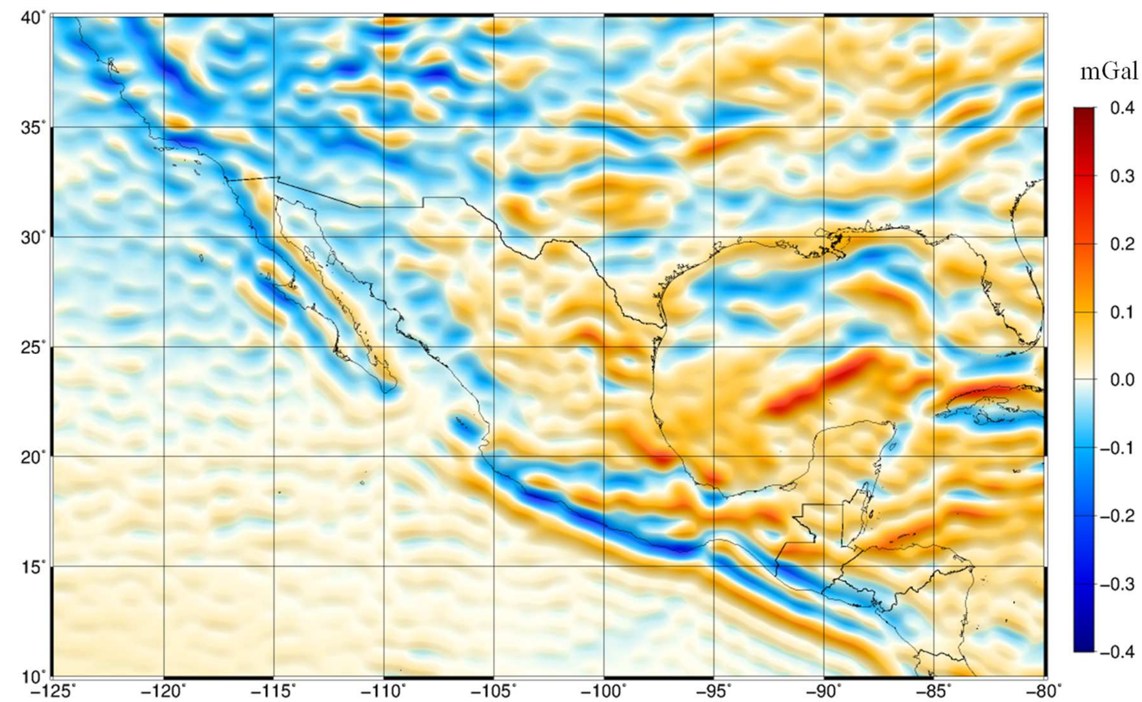

Figure 4.8: Map of ellipsoidal correction for gravity disturbance ($\varepsilon_{\delta g}$).

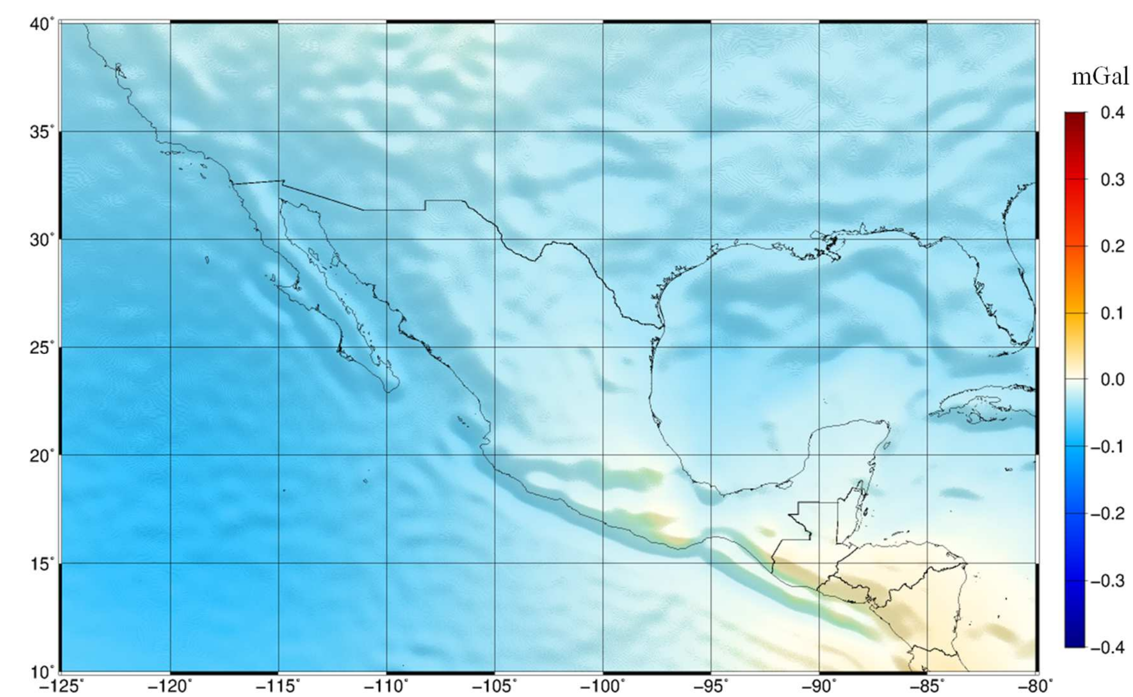

Figure 4.9: Map of ellipsoidal correction for the spherical approximation (ε_n).

The final result of data preparation is the model of Helmert gravity anomalies on the geoid, i.e. the boundary values, presented in Figure 4.10

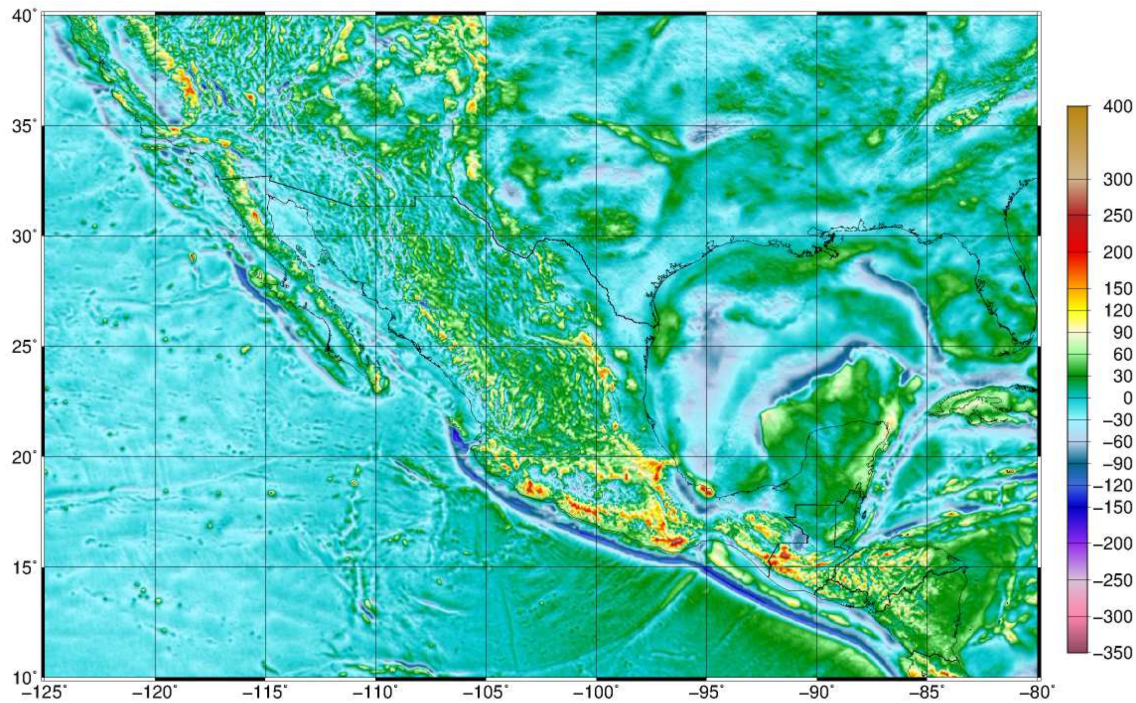

Figure 4.10: Helmert gravity anomaly on the geoid.

Table 4.5. Statistical values for the ellipsoidal corrections and the corrected Helmert gravity anomalies on the geoid. Units mGal.

Statistic	$\varepsilon_{\delta g}$	ε_n	$\Delta g^H(r_g, \Omega)$
mean	0.001	-0.034	-1.725
sigma	0.046	0.023	30.704
max	0.371	0.067	-177.761
min	-0.383	-0.082	342.686

4.3 The modified Stokes integration.

The strategy adopted to apply the Stokes integral consists in taking advantage of the pre-modeled gravity field from satellite observations and focus in processing the residual gravity field. Satellite-only geopotential models, like GOCO06s, are known to be the most accurate source to model the lower frequencies of the gravity field today, but such characteristic fades at the so-called middle-frequencies (e.g., Gruber et al., 2019; Kvas et al., 2021). For this reason it is important to determine a convenient limit to the degree and order of the spherical harmonics frequency to which the pre-modeled gravity field should be used and consider the rest as part of the residual field.

The limit mentioned (L) can be determined from recommendations casted in previous studies about the quality assessment of the geopotential model that has been chosen. In the case of this work, the limit selection was made differently. Applying the procedure proposed by Foroughi et al., 2015, it was performed an analysis of local coherence between the available harmonic coefficients of the model GOCO06s and the GNSS/leveling points available in Mexico. It was decided to test on 20 different choices of the frequency limit of the geopotential model: $L = 60, 70, \dots, 250$. The integration radius of the near-zone was kept fixed as $\psi_0 = 6°$.

The procedure mentioned proposes to generate alternative geoid models, each for every value L to be tested. This implies generating firstly a set of 20 reference gravity field ($\Delta g_{g,L}^H$) and reference spheroids (N_L^H), plus corresponding 20 models of residual gravity ($\delta\Delta g_g^H$) according to 2.17, and another 20 models of residual cogeoid (δN_L^H). Next is presented the result of these alternative solutions.

4.3.1 Reference gravity field and spheroid

Spherical harmonic coefficients of the geopotential model GOCO06s were first reduced to represent the reference disturbing potential (T_L) by subtracting the corresponding coefficients of normal potential. Secondly, the harmonic coefficients of the squared heights model HnmJGP95 were used to compute the reference direct topographical effect on gravity (DTE_L), as in equation 2.17, the reference secondary indirect topographical effect ($SITE_L$) and the reference primary indirect topographical effect ($PITE_L$). Thirdly, the disturbing potential was transformed in reference gravity anomaly using the fundamental gravimetric equation (Vaníček and Krakiwsky, 1986),

$$\Delta g_L\ (r_t, \Omega) \doteq -\frac{\partial T_L}{\partial H} + \frac{1}{\gamma_0}\frac{\partial \gamma}{\partial H} T_L\ , \tag{4.6}$$

and then Helmertized adding DTE_L and $SITE_L$ to obtain Δg_L^H. The fourth step is reserved to compute the reference spheroid (N_L^H), which is derived from the disturbing potential, dividing it over normal gravity and subtracting $PITE_L$. And finally, a degree-zero correction was calculated and added to the reference spheroid to switch the absolute reference of the geoid from the potential reference value $W_0 = U_0 = 6263686.085 m^2 s^{-2}$ to the conventional value used in North America $W_0^{NA} = 6263656.0 m^2 s^{-2}$. This calculation corresponds to equation 2.24. As the results obtained in this stage are too many to be shown, only an example is presented in figures 4.11, 4.12, 4.13, and Table 4.6. This example corresponds to case $L = 230$, a selected value obtained from the analysis in Section 5.1.

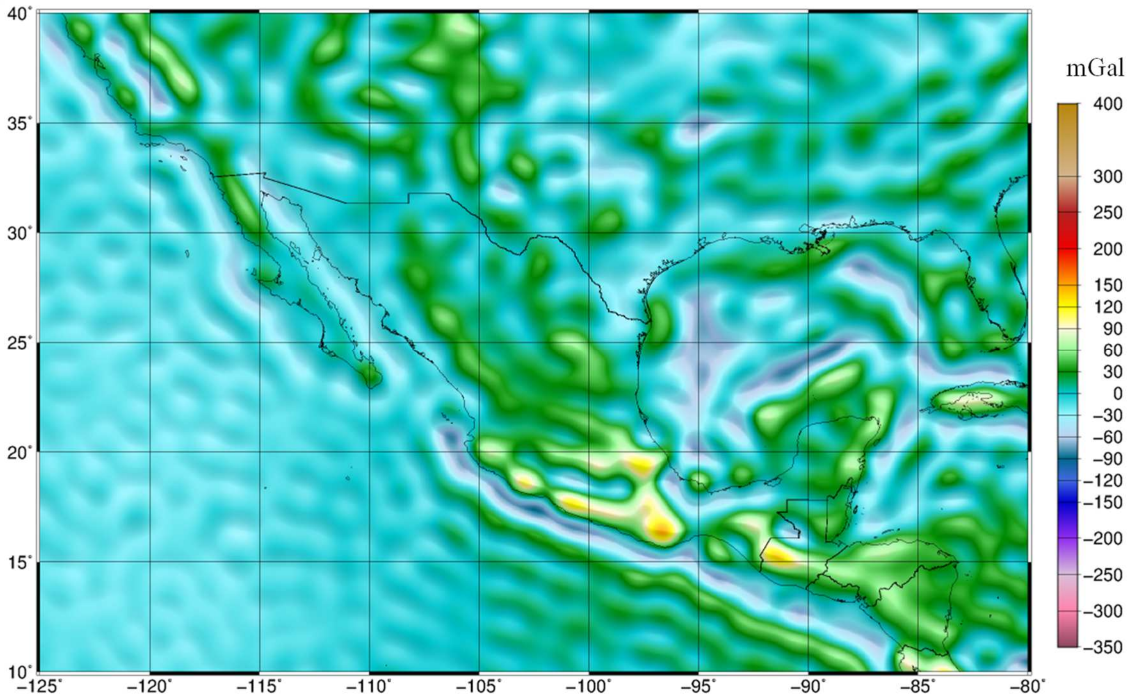

Figure 4.11. Reference gravity field in Helmert space (Δg^{H}_{230}).

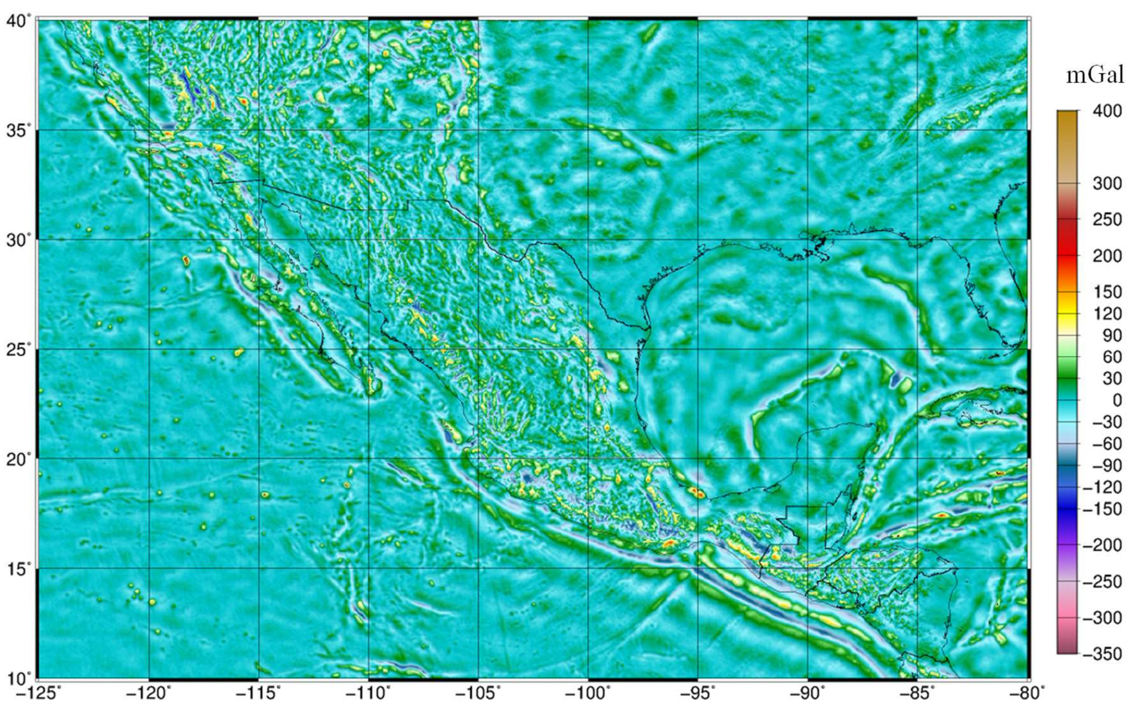

Figure 4.12. Residual Helmert gravity anomaly, $\delta\Delta g^{H}(L = 230)$.

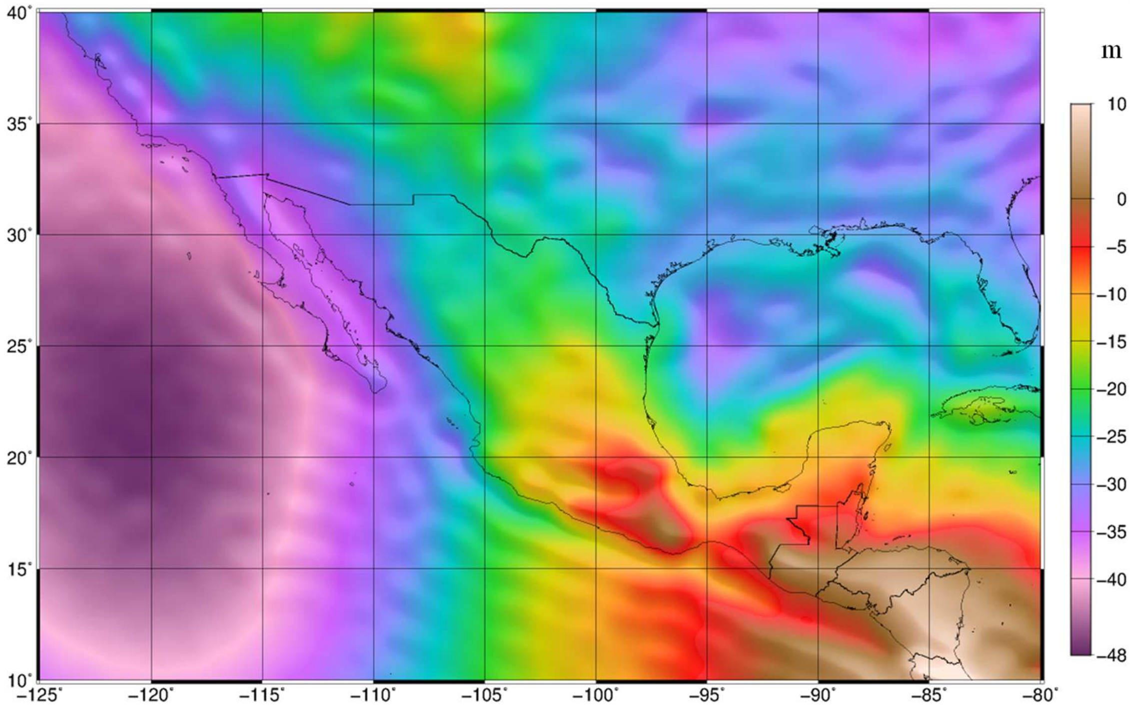

Figure 4.13. Reference spheroid in Helmert space, N_{230}^{H}.

Table 4.6: Statistical values for the Helmertized reference quantities obtained from the GOCO06s model up to degree 230, together with the corresponding residual gravity field.

Statistic	Reference gravity anomaly [mGal]	Residual gravity anomaly [mGal]	Reference spheroid [m]
mean	-2.405	0.328	-26.076
sigma	28.101	20.645	13.040
max	304.437	198.914	13.923
min	-193.171	-171.707	-47.680

4.3.2 Residual cogeoid

The modified Stokes integral was applied on a large spherical cap of radius $\psi_0 = 6°$, which ensures a high accuracy in the computation of the near-zone of influence and yields a minimal contribution from the far-zone for all the higher modification degrees of the test (e.g., Vaníček and Featherstone, 1998). There was a total of 20 residual geoid models produced. Table 4.7 shows a sample of the statistical results obtained in four of the twenty models and Figure 4.14 presents the map of δN^H.

Table 4.7: Statistical values for the residual cogeoid from different modification degrees.

Statistic	$N^H(L = 60)$	$N^H(L = 120)$	$N^H(L = 180)$	$N^H(L = 230)$
mean	0.001	0.003	0.001	0.001
sigma	1.169	0.704	0.452	0.337
max	7.210	5.722	3.898	2.805
min	-5.534	-4.349	-2.786	-2.112

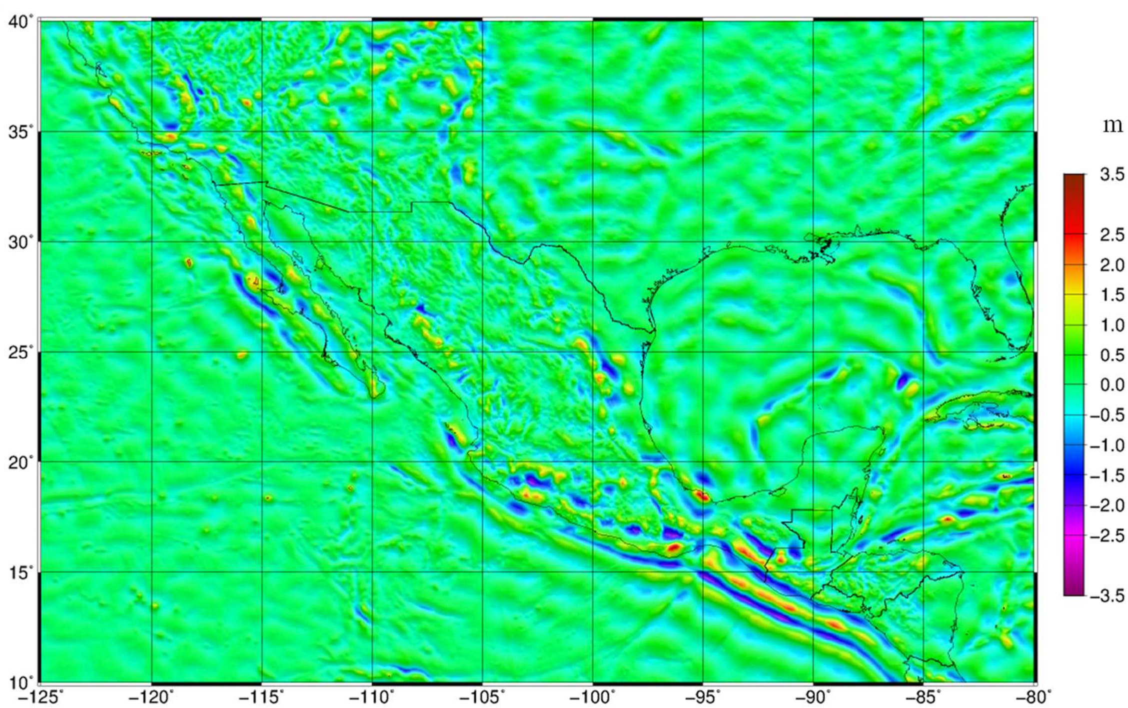

Figure 4.14: Residual cogeoid of degree L=230 (δN^H).

The last step in the strategy to develop the Stokes integral, the cogeoid is obtained by adding the contributions from the reference spheroid and the residual cogeoid. This is:

$$N^H = N_L^H + \delta N_L^H \tag{4.6}$$

The difference among the 20 cogeoid models is in the decimeter level. The model that showed the best precision uses a reference spheroid of degree and order 230. Chapter 5 presents in detail the assessment.

4.4 De-helmertization of the cogeoid.

Regardless of the parameter L chosen to construct a cogeoid model, the primary indirect topographical effect was used as a unique transformation tool to transfer back to the real space all of the cogeoid models produced. See Figure 4.15 and Table 4.8 for reference. Just as well as all other effects presented, the values in this model represent the mean PITE for every cell of coverage 2.5 x 2.5 arc minutes and the coordinate given to such value corresponds to the middle coordinate of the cell.

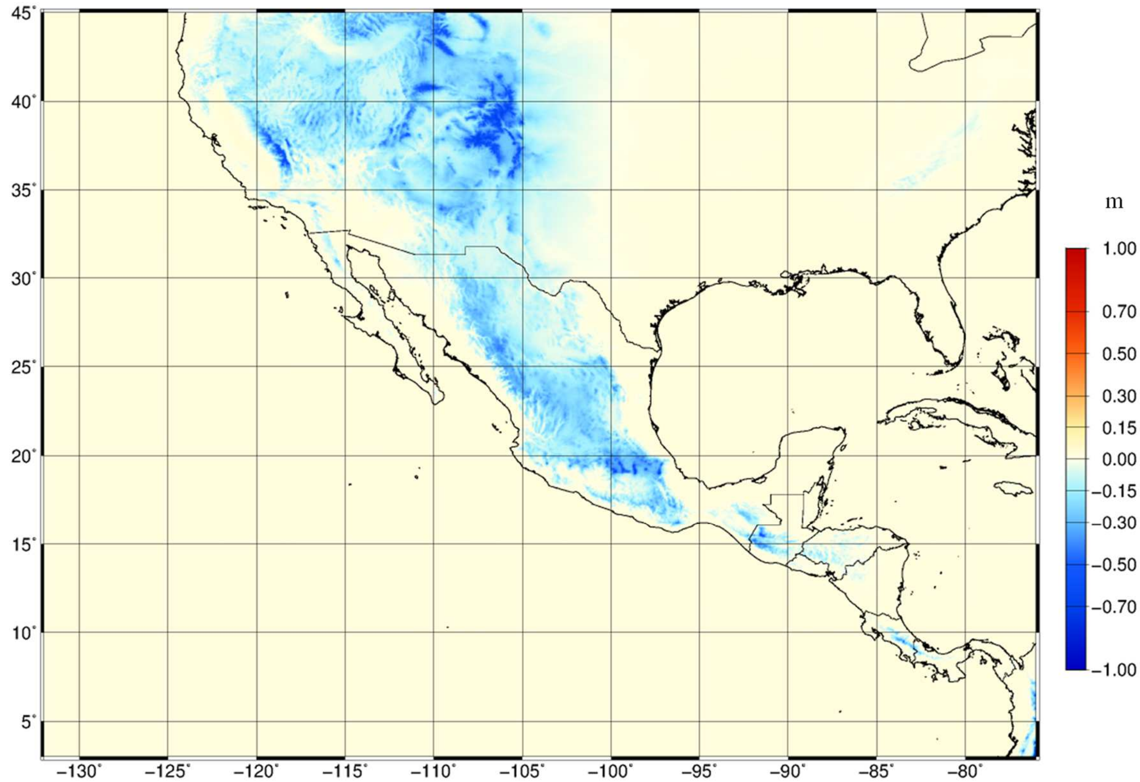

Figure 4.15. Map of the primary indirect topographical effect.

Table 4.8: Statistical values for the primary indirect topographical effect. Units m.

Statistic	PITE
mean	-0.049
sigma	0.082
max	-0.013
min	-0.897

Chapter 5: The geoid model

There was a set of 20 geoid models produced, all using the same input data, parameters and computational technique. The only difference among them is the degree and order of the reference spheroid used. According to the recommendation from Foroughi et al., 2016, the optimal solution can be identified by assessing the geoid models with reference geoidal heights derived from GNSS observations on first order leveling control points. The final geoid model is presented in this chapter as the result from this test and its characteristics are explored.

5.1 Determining the optimal degree of the reference field

Four datasets of precise GNSS observations on leveling benchmarks were collected to serve as reference to identify the geoid model of best precision. Figure 5.3 shows the distribution of these datasets, described in Chapter 3.

Next, the comparison of modeled geoidal height, from each of the 20 models, to the four datasets produced. The differences are summarized in Figure 5.1, separated for every GNSS dataset in terms of standard deviation ($L_2\ norm$).

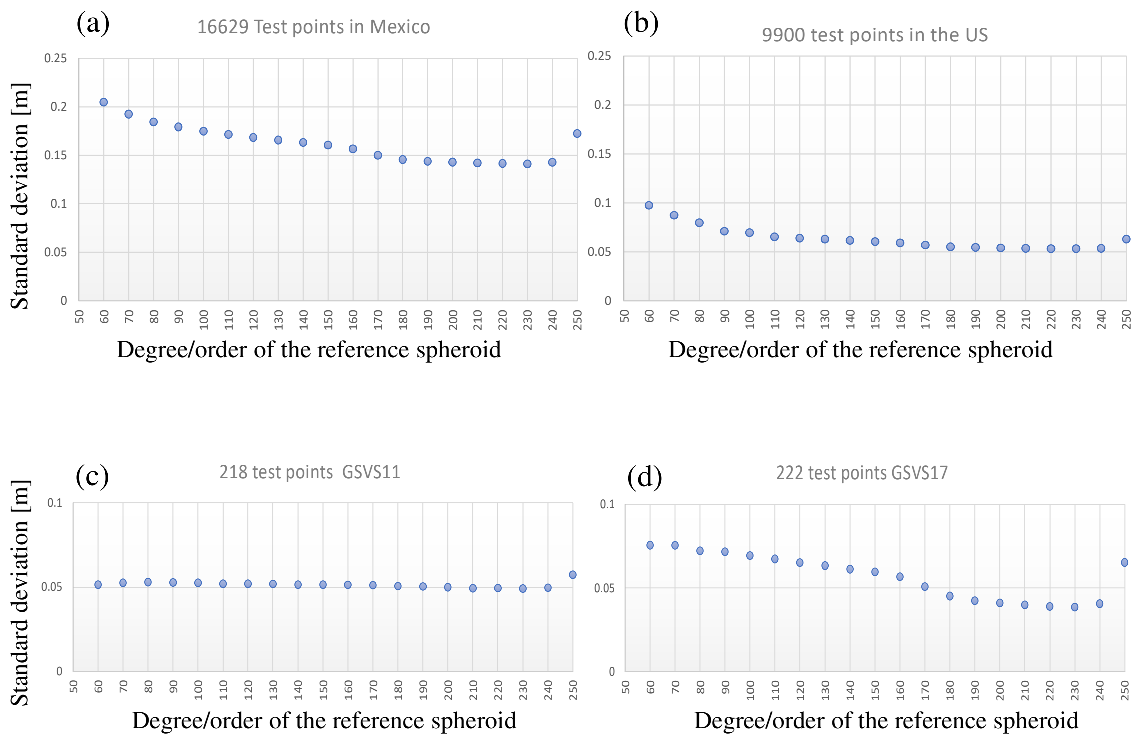

Figure 5.1: Standard deviation of the difference in geoidal height.

It can be noticed from the plots in Figure 5.1, that in all four cases the geoid model improves its coherence with GNSS/leveling data when the degree of reference spheroid increases. Nonetheless, such improvement fades after degree 180 or 200. In all four cases the minimum standard deviation is reached at degree 230 and, therefore, this was the combination chosen to set the final geoid model.

5.2 The geoid model xGGM23

The definitive geoid model for Mexico, identified as xGGM23, is a purely gravimetric solution, optimally combining satellite and terrestrial gravity observations. The satellite-only model GOCO06s is taken as a base pre-modeled solution, transformed to tide-free system for the low frequencies of the spectrum, from degree and order zero to 230 of the spherical harmonic expansion, while the rest of the spectrum is modeled by the sole influence of terrestrial surveys on land and satellite altimetry on the oceans. The coverage ranges 10° to 40° in latitude and 235° to 280° in longitude. The array of geoidal heights provided represent the estimate of mean value over areas covering 2.5 arc minutes in latitude and longitude. The vertical reference of geoidal height is the geodetic ellipsoid GRS80 in reference frame ITRF 2008 and the level surface represented by this geoid model corresponds to the Earth's gravity potential $62636856.0 m^2 s^{-2}$. Regarding the reference epoch, the model is catalogued as "single epoch" or "longtime model", since it was created from input gravity data spanning from the years 1960's to 2020, treating them as simultaneous observations.

From this point in the document, the new geoid model for Mexico is referred to as xGGM23, which stands for "experimental gravimetric geoid for Mexico 2023".

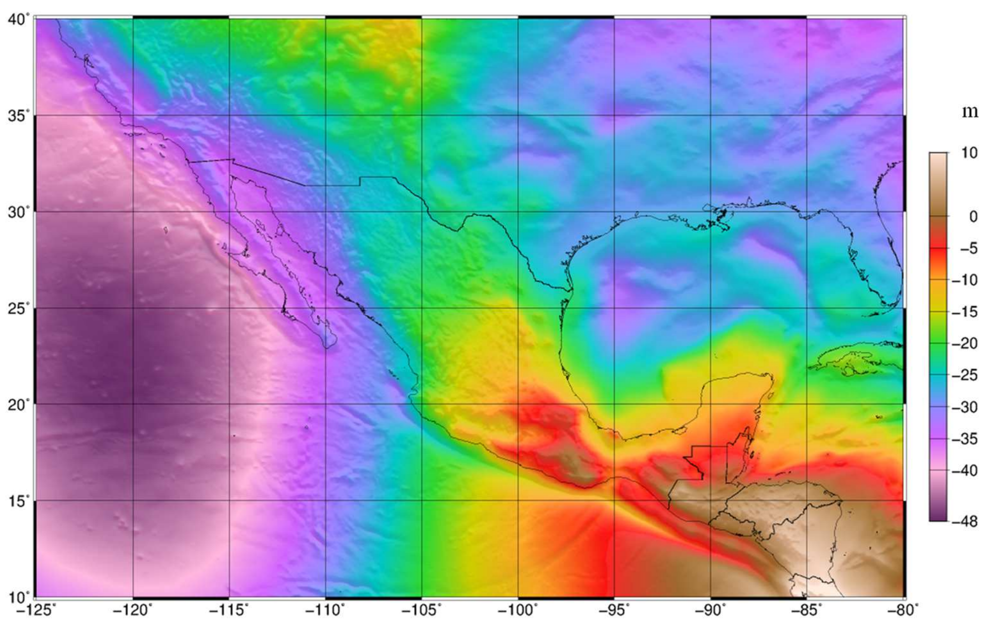

Figure 5.2: The geoid model for Mexico, xGGM23.

Table 5.1: Statistical values of geoidal height. Units [m].

Statistic	Geoidal height (N)
mean	-26.124
sigma	13.026
max	14.626
min	-47.729

The parameterization of the geoid model complies with the convention promoted formal agreement between the geodetic agencies of Canada and the US for the regional geoid for North America (e.g. NGS, 2013; Veronneau and Huang, 2016). It is additionally coincident with the 2003 International Earth Rotation and Reference Frames Service conventions (McCarthy and Petit, 2004). This parameterization can be switched to comply with a different convention. For instance, to make it comply with the International Height Reference System (Sanchez et al., 2021) it is necessary to add a constant value of 26.5 cm to all geoidal heights and add the effect of tide system difference, from tide-free to zero-tide, which varies from 0 to 3 cm (latitude-dependent) over Mexico. Another transformation of interest could be fitting to the mean sea level of tide gauge in Rimouski, Canada, to resemble the original reference of NAVD88. In this case the geoidal heights should be diminished by 32 cm.

5.3 Assessment

Four datasets of geodetic GNSS/leveling were used to analyze the performance of model XGGM23. One of them is the most significant because it is located inside Mexico and realizes the official vertical datum. The remaining three datasets, located in the US, are considered as independent validation tools of higher quality than those existing in Mexico. Additionally, it is presented a comparison with the latest experimental geoid model generated by the US National Geodetic Survey to learn about the general agreement with North American standards.

5.3.1 Comparison with GNSS/leveling data.

Independently from the comparisons made before to determine the optimum degree of the reference spheroid, an assessment is necessary to estimate the the actual precision of the new geoid model. In this section, the data used as reference for the assessment are the four GNSS/leveling datasets described in Chapter 3 with the following characteristics:

Table 5.2: General characteristics of the GNSS/leveling datasets.

Dataset	Mexico	US	GSVS11	GSVS17
Datum	NAVD88-Mx15	NAVD88-detrended	NAVD88	NAVD88
Total points	16629	9900	218	222
Typical error (h)	9 cm	1 cm	0.4 cm	0.4 cm
Typical error (H)	3 mm $\sqrt{k}$	3 mm $\sqrt{k}$	0.7 mm $\sqrt{k}$	0.7 mm $\sqrt{k}$

Although it is also recommended to make use of rigorous orthometric heights for the leveling control to improve the congruency of the height system, in this study it was used the Helmert approximation to orthometric heights as it was obtained from the geodetic national agencies in US and Mexico.

The reference geoidal height from terrestrial surveys was obtained using this formula:

$$N_{GNSS} = h_{GNSS} - H_{Leveling} \tag{5.1}$$

Comparing the point GNSS-derived geoidal heights to the mean values modeled, the difference ($dN = N_{model} - N_{GNSS}$) is summarized in Table 5.3. Units [m].

Table 5.3: Statistical values of geoidal height error estimated from different sources.

Statistic	Mexico	US	GSVS11	GSVS17
Mean	0.363	-0.011	0.316	0.608
Standard deviation	0.141	0.052	0.049	0.034
Maximum	1.111	0.558	0.402	0.690
Minimum	-0.621	-0.546	0.144	0.513

The mean values in Table 5.3 represent the mean datum difference of each model with respect to the datum in every GNSS/leveling dataset. Although the leveling datasets of Mexico and the calibration lines are referred to the same datum, their respective mean is significantly different from each other due to well-known distortion in the NAVD88. This can be confirmed with additional information in the next section. Now, figures 5.3 and 5.4 present a map and profiles of detrended difference, i.e., point differences after removing the bias to see them centered in zero and making it easier to focus on the dispersion.

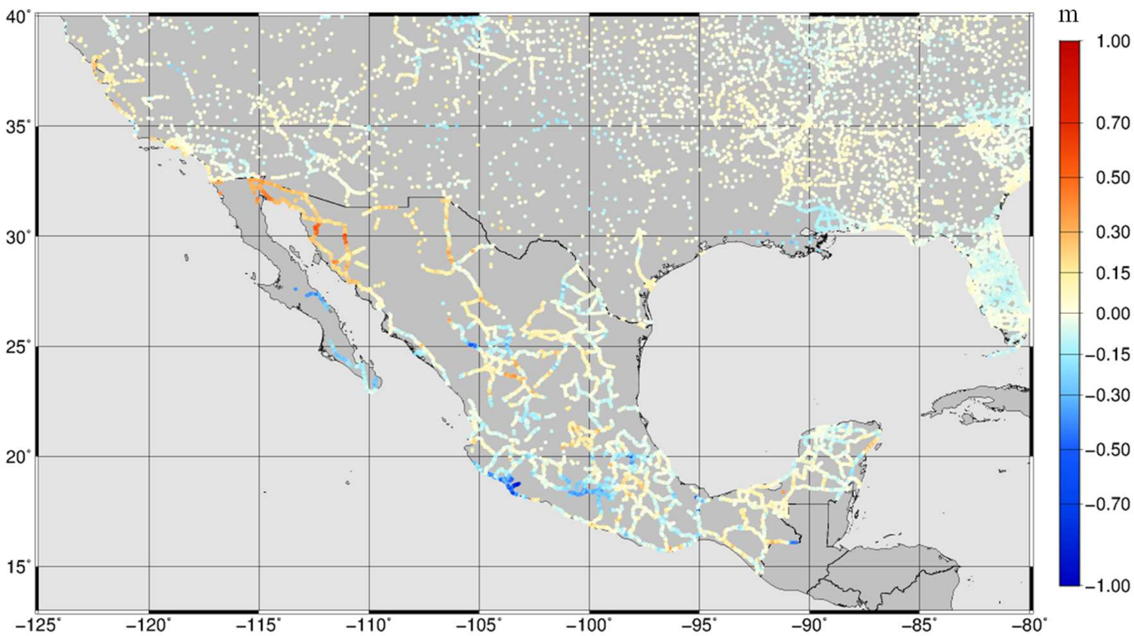

Figure 5.3. Geoidal height difference on national GNSS/Leveling datasets. Units [m].

It can be noticed from Figure 5.3 that the geoidal height difference is smoother in the US territory. The difference grows locally in Mexico to decimeter level but shows no correlation with topography. The areas showing the most notorious difference are (a) Sonora in north-western Mexico with the geoid model higher by some 30 to 40 cm, (b) Colima on the central west coast, where the geoid model is half meter below, and (c) Guerrero in central Mexico with 30 cm below. A few other smaller areas present similarly large difference in the states of Baja California Sur, Durango, Hidalgo and Chiapas.

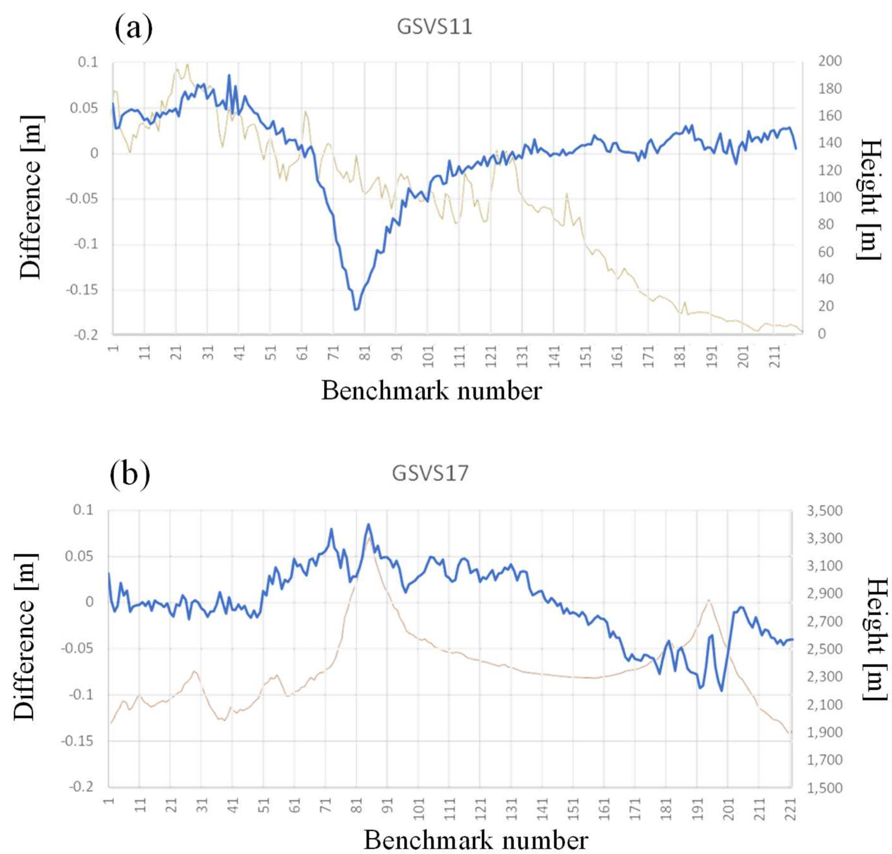

Figure 5.4. Geoidal height difference on the calibration lines (blue line) and corresponding orthometric height (light brown line).

For the case of calibration lines, it can be confirmed that the error in geoidal height is uncorrelated to topography. In line GSVS11, the geoid seems to be affected by a large signal around benchmark 78. The reason for this hasn't been identified. As for the line GSVS17, the estimated error is comparable to the error obtained by those recent geoid models presented in the 1 cm geoid experiment (Wang et al., 2021).

5.3.2 Comparison with independent solutions.

It is presented in this section the result of a new assessment on three geoid models relevant for Mexico: a) GGM10, which is currently distributed by INEGI (INEGI, 2015); b) GGM-CA-2015, produced by the Pan American Institute of Geography and History under leadership of INEGI (Avalos et al., 2016); and c) xGeoid20A, the latest experimental geoid produced by collaboration between NGS and CGS (Wang et al., 2022). The first two were created with a Stokes-Helmert technique and the last one was created under Molodenski's theory.

In its original format, the model xGeoid2020 covers North America with a resolution of 1 arc minute. Every geoidal height corresponds to the estimated point value at the corners of every cell of size $1' \times 1'$. In order to perform a fair comparison with the rest of the models, the geoidal heights from xGeoid2020 where firstly sampled on a dense grid of resolution 0.5 arc minutes using a bilinear interpolation. Secondly the grid was generalized by averaging the 25 sample points found inside every cell of size $2.5' \times 2.5'$, assigning the coordinates for very mean value to the cell-center.

Taking as reference only the GNSS/leveling data in Mexico, Table 5.4 summarizes the result of comparisons, including the statistics obtained from the new geoid model xGGM23.

Table 5.4: Statistical error computed as difference: $dN = N_{model} - N_{GNSS}$, for 16629 points in Mexico. Units [m].

Statistic	GGM10	GGM-CA-2015	xGeoid20A	xGGM23
Mean	0.466	0.342	0.373	0.410
Std.Dev.	0.252	0.202	0.167	0.141
Maximum	1.558	1.454	1.217	1.157
Minimum	-0.734	-0.432	-0.473	-0.570

It can be confirmed from Table 5.4 that the new geoid model performs better than previous regional solutions. However, it is necessary to consider those statistics "pessimistic", due to the following two facts related to the reference point values:

a) Geodetic heights from GNSS surveys in Mexico are characterized by a typical error of $\sigma_h = 0.09$ m.
b) No specific figures are given to the typical error in orthometric heights from leveling or to the amplitude of datum distortions.

Assuming that errors are normally distributed and the combined error of GNSS and Leveling is $\sigma_{h-H} = 0.1$ m, then the actual error estimates ($\sigma_{\delta N}$), presented as standard deviations in Table 5.4, can be decomposed with the following statistical law of error propagation:

$$\sigma_{\delta N}^2 = \sigma_{Nmodel}^2 + \sigma_{h-H}^2 \quad \Rightarrow \quad \sigma_{Nmodel} = \sqrt{\sigma_{\delta N}^2 - \sigma_{h-H}^2} \tag{5.2}$$

Therefore, the final error estimate of the four geoid models is presented next:

Table 5.5: Error estimate for different geoid models inside Mexico.

	GGM10	GGM-CA-2015	xGeoid20A	xGGM23
Estimated error [m]	0.231	0.176	0.134	0.099

These figures about the error in geoid models can be considered realistic, or even slightly pessimistic; firstly because the errors in leveling were assumed to be of minimal influence, and secondly, because the statistics over a large area of the US territory is nearly half of the one calculated here for the model xGGM23. Considering that the GNSS control in the US is more reliable and the input data in Mexico and the US of similar quality, it is expected that the accuracy of the geoid model should be similar in both countries.

Lastly in this section, it is presented the comparison between the two most precise models as an additional tool for analysis.

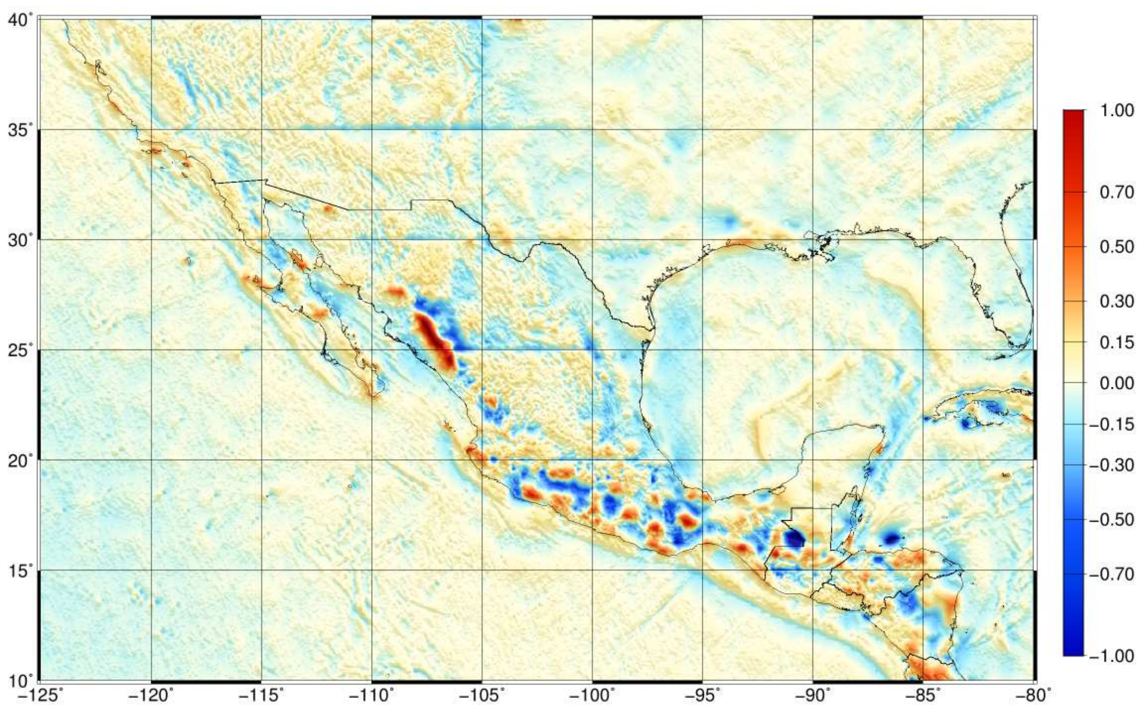

Figure 5.5. Difference of geoidal height: $dN = N_{xGGM23} - N_{xGeoid20A}$.

Most notable differences in Figure 5.5 correspond to input gravity data-gaps in one or both models. Nonetheless, it is important to notice that a middle-size signal of nearly 15 cm of amplitude crosses all over the map, including the oceans. The source of this signal has not been identified.

It can be also noticed that the magnitude of differences is uncorrelated to topographic heights or national boundaries. Interestingly, looking side-by-side the maps of Figure 5.6 and Figure 5.4, the area by the western side of the Mexico-US border shows a clearly different behavior. While the geoid models show good agreement across the national border, the comparison of GNSS/leveling data present a clear pattern of systematic difference of nearly 30 cm inside Mexico. This could be an indication of distortion in the leveling datum of Mexico.

6 Chapter 6: Conclusions and Recommendations

6.1 Conclusions

The Stokes-Helmert technique for geoid computation has been applied successfully over Mexico and its surrounding area. Details of the technique have been described in accordance with the current status of theory and computational development. More than a million terrestrial gravity observations have been collected, analyzed and processed. Digital elevation models and parameterization needed for the geoid modeling was taken from the recommendations of the IAG Sub-Commission 2.4c, Regional Geoid for North and Central America.

Within the processing strategy, the preparation of the grid of Helmert gravity anomalies referred to the geoid level was achieved through several steps, summarized as follows: the gridding of gravity observations was performed using a prediction algorithm on gravity anomalies expressed in the No-Topography space; i.e., on spherical complete Bouguer anomaly at the surface. Program gravgrid.c was created to perform this operation, including the estimate of precision for every predicted mean gravity value. Subsequently, the grid was transformed to the Helmert space by adding the effect on gravity of condensed topography, using the second Helmert's condensation scheme to preserve the center of mass collocated at the origin of the coordinates system (e.g. Ellmann and Vaníček , 2007). Finally, it was performed a downward continuation based on the classical approach of the Poisson integral applied iteratively, using the Jacobi method with the convergence criteria proposed by Kingdon and Vaníček (2010). Finally, the two ellipsoidal corrections were computed according to the description of Section 2.4 and added to the result of downward continuation.

The geoid computation was produced in the Helmert space, using the Stokes' integral on a residual gravity field, spectrally separated from the lower frequencies at degree and order 230 of the spherical harmonics. This integral's kernel was also modified to minimize the impact of the global gravity field, according to the modification scheme by Vaníček and Kleusberg (1986). The integral was evaluated separately for a near-zone spherical cap of radius $\psi_0 = 6°$ and the remaining far-zone beyond this radius (known as truncation error). As a result, the residual geoidal height was combined with a reference spheroid of maximum degree and order 230, derived from pre-modeled Earth's gravity potential of satellite observations. Such number is an optimal value derived from analysis of the precision of the geoid model over Mexico and a large portion of the US territory. Model GOCO06s (Kvas et al., 2021) was Helmertized to conform the reference spheroid and reference gravity field from degree and order 0 to 230. Program Helmert_ref.c was created to perform this operation while selecting the absolute reference value W_0 according to the regional standard for North America. Finally, the cogeoid was completed adding the residual cogeoid from the Stokes integral to the reference spheroid.

Last step of the Stokes-Helmert method was done calculating a refined primary indirect topographical effect and adding it to the cogeoid in order to de-helmertize it. The final geoid model was named xGGM23, which stands for "experimental gravimetric geoid for Mexico 2023". Maps and statistical results were provided to describe the geoid model as well as all its intermediate calculation steps.

The xGGM23 was assessed with terrestrial GNSS observations on the national leveling network of Mexico. Its precision was realistically estimated in 10 cm of standard deviation inside Mexico, which doubles the precision of the model GGM10 in practical use and outperforms by 34% the precision achieved by the model xGeoid20A in this territory. Additionally, the reliability of the new geoid model was confirmed by applying the same computation technique on the US territory, where the precision of GNSS-derived heights is better, and the agreement between GNSS/leveling data and the geoid is in the order of 5 cm standard deviation.

Local discrepancies remain in Mexico, higher than 10 cm between GNSS/leveling data and the geoid, some of which could be part of geoid-error and some part of leveling network distortions. There were no specific results presented towards the clarification of the error source between these two vertical references.

6.2 Recommendations

Three specific activities can be pointed out for future work, derived from the experience in computing the geoid model for Mexico.

(a) Refinements of the geoid calculation can be sought by considering the contribution of anomalous topographical density to direct and indirect topographical effects (e.g. Huang et al., 2001; Foroughi et al., 2015b).

(b) Using rigorous orthometric height for the national leveling networks is expected to increase the coherence between the gravimetric geoid and the leveling datum (e.g. Santos et al., 2006; Foroughi et al., 2018).

(c) It is advisable to investigate the source of the local feature presented in the geoid assessment on the calibration line GSVS11, which introduces an error larger than 10 cm in the geoid model. This could lead to finding a general improvement to the model.

Reference list

Andersen, O., Knudsen, P., Kenyon, S., Holmes, S. and Factor, J. K. (2019). Evaluation of the Global Altimetric Marine Gravity Field DTU15: Using Marine Gravity and GOCE Satellite Gravity. In L. Sánchez, & J. T. Freymueller (Eds.), International Symposium on Advancing Geodesy in a Changing World - Proceedings of the IAG Scientific Assembly, 2017 (pp. 77-81). Springer. International Association of Geodesy Symposia Vol. 149 https://doi.org/10.1007/1345_2018_52

Ahlgren, K.M., Scott, G., Zilkoski, D., Shaw, B. and Paudel, N. (2020) GEOID18. NOAA Technical Report NOS NGS, 72. Silver Spring, Maryland.

Avalos-Naranjo, D., Sosa-Gaytán, M. and Mendoza-Martínez, MA. (2016a). La red nodal para control geodesico vertical del INEGI. Internal report of the Instituto Nacional de Estadística y Geografía. Aguascalientes, México.

Avalos-Naranjo, D., Muñoz-Abundes, R., Ballesteros, C., Medrano-Silva, W., Alvarez-Calderon, A., Figueroa, C., Robles-Pereira, V., Meza, O. and Taveras, L. (2016b). El modelo geoidal regional GGM-CA-2015, resultados y experiencia de la cooperación técnica en la región México, Centroamérica y el Caribe. Revista Cartografica 92. DOI 10.35424/rcarto.i92.448

Bursa, M. (1999). Determination of the geopotential at the tide gauge defining the north american vertical datum 1988 (NAVD88). Geomatica, Volume 53.

Brown, N. J., McCubbine, J. C., Featherstone, W. E., Gowans, N., Woods, A. and Baran, I. (2018). AUSGeoid2020 combined gravimetric–geometric model: location-specific uncertainties and baseline-length-dependent error decorrelation. Journal of Geodesy, 92(12), 1457–1465.

Ellmann, A., Tenzer, R. and Janak, J. (2005). Stokes-Helmert’s Geoid software reference manual. University of New Brunswick, Canada.

Ellmann, A. and Vaníček, P. (2007). UNB application of Stokes-Helmert's approach to geoid computation. Journal of Geodynamics, 43, 200-213.

Foroughi I., Janák J., Kingdon R., Sheng M., Santos M. and Vaníček P. (2015a). Illustration of how satellite global field should be treated in regional precise geoid modelling (Padding of terrestrial gravity data to improve Stokes-Helmert geoid computation). Presented at the EGU General Assembly 2015. Vienna.

Foroughi, I., Sheng, M., Kingdon, R., Huang, J., Martinec, Z. and Vaníček, P. (2015b). The effect of lateral topographical density variations on the geoid in Auvergne. 26th IUGG General Assembly, Prague, Czech Republic.

Foroughi, I., Vaníček, P., Novák, P., Kingdon, R., Sheng, M., and Santos, M. (2016). Optimal combination of satellite and terrestrial gravity data for regional geoid determination using Stokes-Helmert's method. IAG proceeding. Thessaloniki, Greece.

Foroughi, I., Vaníček, P., Kingdon, R.W., Goli, M., Sheng, M., Afrasteh, Y., Novák, P. and Santos, M. (2018a). Sub-centimtre geoid. Journal of Geodesy. DOI 10.1007/s00190-018-1208-1.

Foroughi, I. (2018b). Accuracy of the classical height system. Technical report 316, the Department of Geodesy and Geomatics Engineering, University of New Brunswick.

Gruber, T., Oikonomidou, X., Bruinsma, S., Visser, P. and Mulet, S. (2019). Release 6 GOCE Gravity Field Models Validation Report. The European GOCE Gravity Consortium EGG-C. Document id: GO-TN-HPF-GS-0337.

Heiskanen, W. and Moritz, H, (1967). Physical Geodesy. San Francisco: W.H. Freeman and Co.

INEGI (2015). El geoide gravimetrico Mexicano 2010. Instituto Nacional de Estadistica y Geografia, Aguascalientes, Mexico. ISBN 978-607-739-636-9.

INEGI (2016). Cambio al datum vertical NAVD88 en información geodésica oficial. Instituto Nacional de Estadistica y Geografia, Aguascalientes, Mexico.

Kingdon, R. and Vaníček, P. (2010). Poisson downward continuation solution by the Jacobi method. Journal of Geodetic Science, 1, 74-81.

Krcmaric, J. (2022). Development and evaluation of the xGEOID20-DEM at NGS. Presentation of the European Geophysical Union Congress 2022. Vienna, Austria, May 25th, 2022.

Kvas, A., Brockmann, J.M., Krauss, S., Schubert, T.; Gruber, T., Meyer, U., Mayer-Gürr, T.; Schuh, WD., Jäggi, A. and Pail, R. (2021). GOCO06s - a satellite-only global gravity field model. Earth System Science Data, 13(1), 99–118. DOI 10.5194/essd-13-99-2021.

Li, X., Ahlgren, K., Hardy, R., Krcmaric, J. and Wang, Y.M. (2019) The Development and Evaluation of the Experimental Gravimetric Geoid Model 2019, https://beta.ngs.noaa.gov/GEOID/xGEOID19/xGeoid19_tech_details.v10.pdf.

Martinec, Z., Vaníček P., Mainville A. and Véronneau M. (1995) The effect of lake water on geoidal heights. Manuscr Geodaet 20: 193-203.

McCarthy, D.D. and Petit, G. (eds) (2004). IERS conventions (2003).IERS Conventions Centre, IERS Technical Note No. 32, Vlg.des Bundesamts für Kartographie und Geodäsie, Frankfurta. M., 127 pp.

Mendoza-Martínez, M.A. and Avalos-Naranjo, D. (2018). Sobre la exactitud de modelos digitales de terreno SRTM4.1, CEM3.0 y LIDAR-IMAR. Internal report of the Instituto Nacional de Estadística y Geografía. Aguascalientes, México.

Huang, J., Vaníček, P., Pagiatakis, S. and Brink, W. (2001). Effect of topographical mass density variation on gravity and the geoid in the Canadian Rocky mountains. J Geodesy 74: 805-815.

Moritz, H. (1980) Advanced Physical Geodesy, Herbert Wichmann Verlag, Karlsrihe.

Moritz, H. (2000) Geodetic Reference System 1980. Journal of Geodesy 74, 128–133. DOI 10.1007/s001900050278.

National Geodetic Survey. (2013). The National Geodetic Survey ten-year strategic plan, 2013-2023: positioning America for the future. NOAA/National Geodetic Survey, Silver Spring, MD, USA.

Navratil, G. and Unger E.M. (2011). Height Systems for 3D Cadastres. FIG Conference: 2nd International Workshop on 3D Cadastres. TU Delft, The Netherlands.

Pavlis, N.K., Holmes, S.A., Kenyon, S.C. and Factor J.K. (2012). The development and evaluation of the Earth Gravitational Model 2008 (EGM2008). JGR Solid Earth, Volume117, IssueB4.

Pérez, J.L., Mozas, A.T., López, A., Aguilar, F.J., Delgado, J., Fernández, I. and Aguilar, M.A. (2012) Efficient methods to convert LiDAR-derived ellipsoid heights to orthometric heights, International Journal of Applied Earth Observation and Geoinformation, Volume 18, 2012, ISSN 1569-8432. DOI 10.1016/j.jag.2011.09.019.

Pujol, M.I., Schaeffer, P., Faugère, Y., Raynal, M., Dibarboure, G. and Picot, N. (2018). Gauging the improvement of recent mean sea surface models: A new approach for identifying and quantifying their errors. Journal of Geophysical Research: Oceans, 123, 5889–5911. DOI 10.1029/2017JC013503.

Rizzoli P., Martone, M., Gonzalez, C., Wecklich, C., Borla-Tridon, D., Bräutigam, B., Bachmann, M., Schulze, D., Fritz, T., Huber, M., Wessel, B., Krieger, G., Zink, M. and Moreira, A. (2017). Generation and performance assessment of the global TanDEM-X digital elevation model, ISPRS Journal of Photogrammetry and Remote Sensing, Volume 132, 2017, Pages 119-139, ISSN 0924-2716, DOI 10.1016/j.isprsjprs.2017.08.008.

Roman, D.R. (2010). Modernizing the geopotential datum: replacing NAVD88. Proceedings of the 2010 Federal geospatial summit on improving the national spatial reference system. NOAA, Silver Spring, Maryland, May 2010.

Santos, M., Vaníček, P., Featherstone, W., Kingdon, R., Ellmann, A., Martin, B.A. and Tenzer, R. (2006). The relation between rigorous and helmert's definition of orthometric heights. Journal of Geodesy, 80(12), 691–704.

Smith, D.A., Holmes, S.A., Li, X., Guillaume, S., Wang, Y.M., Bürki, B., Roman, D.R. and Damiani, T.M. (2013). Confirming regional 1 cm differential geoid accuracy from airborne gravimetry: the Geoid Slope Validation Survey of 2011. J Geod 87:885–907. DOI 10.1007/s00190-013-0653-0.

Tenzer, R., Vaníček, P., van Eck van der Sluijs, S. and Hernández-Navarro, A. (2003). On Some Numerical Aspects of Primary Indirect Topographical Effect Computation in the Stokes-Helmert Theory of Geoid Determination. Revista Cartografica, Vol 76-77.

Tenzer R., Novák P., Janák J., Huang J., Najafi M., Vajda P. and Santos M. (2003). A review of the UNB approach for precise geoid determination based on the Stokes-Helmert method. Honoring the academic life of Petr Vaníček. Technical Report No. 218, University of New Brunswick, Fredericton, pp.132-176.

Torge, W., 2001. Geodesy. De Gruyter, 3rd edition.

United States Geological Survey (2021). 3D Elevation Program 1-Meter Resolution Digital Elevation Model (published 20200606), accessed October 23, 2021 at URL https://www.usgs.gov/the-national-map-data-delivery DOI 10.5069/G98K778D.

Vaníček, P. and Krakiwsky, E. (1986). Geodesy, The concepts. Amsterdam, North Holland.

Vaníček, P. and A. Kleusberg (1987). The Canadian geoid – Stokesian approach. Manuscripta Geodaetica 12:86-98. Springer Verlag 1987.

Vaníček , P. and Sjoberg, L.E., 1991. Reformulation of Stokes's theory for higher than second-degree reference field and modification of integration kernels. J. Geophys. Res. 96 (B4), 6339–6529.

Vaníček, P., Najafi, M., Martinec, Z., Harrie, L. and Sjoberg, L. E. (1995). High-degree reference field in the generalized Stokes-Helmert scheme for geoid computations. Journal of Geodesy (70): 176-182.

Vaníček , P. and Featherstone, W.E. (1998). Performance of three types of Stokes's kernel in the combined solution for the geoid. Journal of Geodesy 72. Springer Verlag, 1998.

Vaníček , P., Huang, J., Novák, P., Pagiatakis, S.D., Veronneau, M., Martinec, Z. and Featherstone, W.E. (1999). Determination of the boundary values for the Stokes–Helmert problem. J. Geodesy 73, 160–192.

van Westrum, D., Ahlgren, K., Hirt, C. and Guillaume, S. (2021). A Geoid Slope Validation Survey (2017) in the rugged terrain of Colorado, USA. Journal of Geodesy 95, 9 (2021). https://doi.org/10.1007/s00190-020-01463-8

Véronneau M. and J. Huang (2016). The Canadian Geodetic Vertical Datum of 2013 (CGVD2013), GEOMATICA, Vol. 70, No. 1, pp. 9-19, doi:/10.5623/cig2016-101

Yamazak, D., Ikeshima, D., Tawatari, R., Yamaguchi, T., O'Loughlin, F., Neal, JC., Sampson, CC., Kanae, S. and Bates, BD., (2017): A high accuracy map of global terrain elevations, Geophysical Research Letters, vol.44, pp.5844-5853.

Yang, H., Tenzer, R., Vanícek, P. and Santos, M. (2004). Atmospheric effect in the three-space scenario for the Stokes-Helmert method of geoid determination. Poster presentation of the AGU/CGU Joint Assembly, Montreal, Canada.

Wang, Y.M. et al. (2021a) Colorado geoid computation experiment—Overview and summary, Journal of Geodesy 95.12 (2021): 1–21.

Wang, Y.M., Li, X., Ahlgren, K., Krcmaric, J., Hardy, R., Veronneau, M., Huang, J. and Avalos, D. (2022). Technical Details of the Experimental GEOID 2020. NOAA Technical Report NOS NGS 78. June 2022.

Wessel, B., Huber, M., Wohlfart, C., Marschalk, U., Kosmann, D. and Roth, A. (2018). Accuracy Assessment of the Global TanDEM-X Digital Elevation Model with GPS Data. ISPRS Journal of Photogrammetry and Remote Sensing. Vol. 139, pp. 171-182.

Zilkoski, D.B., Richards, J.H. and Young, G.M. (1992). Results of the general adjustment of the North American Vertical Datum of 1988. Surv Land Inf Syst 52(3):133–149.

Zingerle, P., Pail, R., Gruber, T. and Oikonomidou, X. (2020). The combined global gravity field model XGM2019e. Journal of Geodesy 94, article 66 (2020). DOI 10.1007/s00190-020-01398-0.

Appendix I: On the technique for gravity prediction.

This section contains a detailed description of the method implemented to create a grid of predicted mean gravity anomaly, derived from an input set of scattered point observations. The actual result of this method was presented in Chapter 4.

Recently, Dr. P. Vaníček (personal communication, 2022) proposed a strategy to predict gravity values minimizing the risk of error and treating uncertainty of the input data in a formal way to determine the uncertainty of the output. Two computation modes are described: point prediction and cell mean value prediction.

A) Prediction in point mode.

The strategy consists in identifying the existing observations surrounding the point of interest and performing a weighted average with them. The weighting scheme is function of inverse distance. Using a search radius $s = 0.5°$, the total observations found in distance $d < s$ is named K. Then the weight assigned to each of the $k = 1,2,\ldots,K$ observations corresponds to a power (n) of the inverse distance:

$$p_k(n) = 1/d_k^n \;, \tag{A.1}$$

where p_k is function of n and distance d_k. In order to avoid any unintended scaling in the prediction, this set of weights is normalized as follows:

$$p_k{}'(n) = {p_k(n)}\Big/{\sum_{k=1}^{K} p_k(n)} \tag{A.2}$$

Then, arranging the K observations in vector form ($\Delta\boldsymbol{g}$), and their corresponding weight as vector $\boldsymbol{P'}$, the predicted gravity anomaly for an arbitrary position is computed as

$$\widehat{\Delta g} = \boldsymbol{P}'(n)^T \, \Delta\boldsymbol{g} \qquad \text{(A.3)}$$

If the covariance matrix of the K observations is $\boldsymbol{C}$, then the estimated variance of the prediction in the point of interest is computed as follows:

$$\sigma_k^2 = [\boldsymbol{P}'(n)^T \boldsymbol{C} \, \boldsymbol{P}'(n)]^{-1} \qquad \text{(A.4)}$$

When specific information is available about the uncertainty of every observation included in the vector $\Delta\boldsymbol{g}$, then it can be used to fill in the $\boldsymbol{C}$ matrix. As it is often the case, the gravity values available lack of particular and realistic uncertainty estimates. In such cases the estimate of uncertainty (σ) can be calculated using a constant value for all the observations involved, in which case the whole $\boldsymbol{C}$ matrix conforms an identity matrix with a constant factor.

This method should be implemented preferably in the smoothest gravity field that observed gravity can be transformed to. The smoothness of the gravity field is important because it leads to reduced amplitude of the prediction error. Although there may be gravity fields even smoother that the NT-anomaly on the topographic surface ($\Delta g^{NT}(r_t, \Omega)$), in the work presented here, this is the smoothest obtained.

B) Prediction in grid mode.

A predicted mean value ($\widehat{\Delta g}_{\alpha}^{NT}$) corresponds to the average of point predictions sampled regularly inside the area of every cell (α) delimited by constant latitude and longitude steps. Every cell of the grid was assigned with a constant number of m point predictions and then the predicted mean was calculated as simple cell average. A number of tests with this algorithm showed that using power $n = 4$ and a sample of $m = 6 \times 6 = 36$ points result in reliable predictions for cells of area $1' \times 1'$ and $2.5' \times 2.5'$.

The uncertainty of $\widehat{\Delta g}_{\alpha}^{NT}$ was calculated as the mean covariance among the 36 sample points inside the cell α, making use of the σ^2 point values as follows:

$$\sigma_{\alpha}^{2} = \frac{1}{m^2} \sum_{i=1}^{m} \sum_{j=1}^{m} \frac{\sigma_i \sigma_j}{1 + d_{ij}^2} \tag{A.5}$$

where d_{ij} is distance between i^{th} and j^{th} sample points inside the cell α; i.e. $i, j \in \{1,2, \ldots ,36\}$. Figure I.1 shows an example of the covariance values obtained for 36 sample points inside a cell of size $2.5' \times 2.5'$. It is a matrix of dimension 36x36 where the diagonal contains the point covariance described in equation A.4. for which there exists an observed point near the lower right corner of the area, assumed with uncertainty of 1 mGal. In this case, the sample points near the upper-left corner are farther away from other observations and, therefore, the algorithm assigns a higher uncertainty to those. Extreme covariance values are 0.08 and 2.86 mGal in this example.

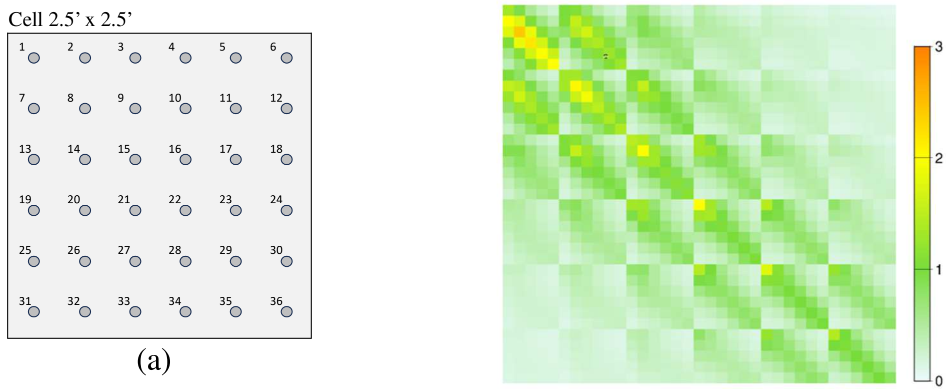

(a) (b)

Figure I.1: Arrangement of the sample point predictions (a), and covariance among the 36 point predictions of gravity anomaly (b).

Results of this method are presented in Chapter 4. By making a direct comparison between every input gravity anomaly value and its corresponding predicted mean value delivers the statistics presented in Figure I.2.

Statistic	Prediction error
mean	0.010
sigma	1.879
max	35.342
min	-79.839

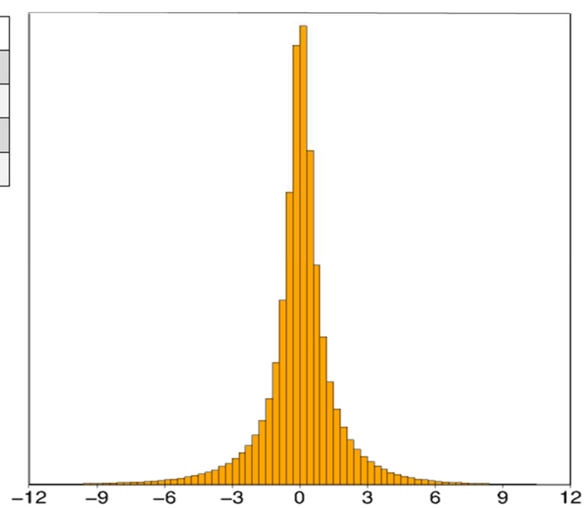

Figure I.2: Histogram and statistical values of the prediction error.

Errors larger than 4σ may be considered as outliers, undetected by the data cleaning process described in Chapter 3. The status of these possible outliers was not investigated.

Curriculum Vitae

Candidate's full name: David Avalos - Naranjo.

Universities attended: Universidad Autónoma de Aguascalientes,
Bachelor of Science, Applied Mathematics, June 1999.

Selected Publications:

- Avalos-Naranjo, D., Muñoz-Abundes, R., Ballesteros, C., Medrano-Silva, W., Alvarez-Calderon, A., Figueroa, C., Robles-Pereira, V., Meza, O., Taveras, L. (2016b). El modelo geoidal regional GGM-CA-2015, resultados y experiencia de la cooperación técnica en la región México, Centroamérica y el Caribe. Revista Cartografica 92. DOI 10.35424/rcarto.i92.448

- Avalos-Naranjo, D., Muñoz-Abundes, R., Ballesteros, C., Medrano-Silva, W., Alvarez-Calderon, A., Figueroa, C., Robles-Pereira, V., Meza, O., Taveras, L. (2013). Diagnostic of geodetic infrastructure for Mexico, Central America and the Caribbean. Revista Cartográfica 89, Pan American Institute of Geography and History, 2013. DOI 10.35424/rcarto.i89.489.

- Avalos, D., M.C. Santos, P. Vaníček and A. Hernandez (2007). Insights Into the Mexican Gravimetric Geoid. Proceedings of the International Union of Geodesy and Geophysics General Assembly, Perugia, Italy, July 2007.

- Avalos-Naranjo, D. (2004). Continuo de Elevaciones Mexicano. Revista Cartografica No. 78/79, Pan American Institute of Geography and History, 2004. ISSN 0080-2085.

- Avalos-Naranjo, D. (2004). Nuevo modelo geoidal Mexicano GGM04. Revista Cartografica No. 78/79, Pan American Institute of Geography and History, 2004.

- Avalos-Naranjo, D. and R. Munoz-Abundes (2005). Estado del geoide gravimétrico mexicano. Revista Cartografica No. 80/81, Pan American Institute of Geography and History, 2005. ISSN 0080-2085.

Selected Conference Presentations:

- An assessment on the Mexico gravity network and its integration to IGRF. IGRF workshop of the International Association of Geodesy, Leipzig, Germany, 2022.

- Experiences of geoid modeling in Mexico. Simposio SIRGAS, Quito, Ecuador 2020.

- Absolute gravity measurements in Mexico for the national geodetic control. Congress of the International Union of Geodesy and Geophysics, Montreal, Canada, 2019.

- Monitoring relative gravimeters performance for quality control in Mexico's gravity data. Poster presentation of the American Geophysical Union Spring Meeting, Mexico, May 2013.

- Effects of tectonic plate deformation en the geodetic reference frame of Mexico. Poster presentation of the American Geophysical Union Spring Meeting, Mexico, May 2013. G33B-04G.

- Towards the re-definition of the gravity network in Mexico. Gravity, Geoid and Height Systems Simposium. Italia, October 2012.

- A study of the Earth crustal movements and its effect on the geodetic control for Mexico. 10º Congreso del Colegio de Ingenieros Topógrafos, Zacatecas, México, Noviembre 2010.